

Self-excited primary and secondary instability of laminar separation bubbles

Daniel Rodríguez^{1,†}, Elmer M. Gennaro² and Leandro F. Souza³

¹ETSIAE-UPM (School of Aeronautics), Universidad Politécnica de Madrid, Plaza del Cardenal Cisneros 3, 28040 Madrid, Spain

²São Paulo State University (UNESP), Campus of São João da Boa Vista, São João da Boa Vista-SP 13876-750, Brazil

³Institute of Mathematical and Computer Sciences, University of São Paulo, São Carlos-SP 13566-590, Brazil

(Received 17 April 2020; revised 6 August 2020; accepted 8 September 2020)

The self-excited instabilities acting on laminar separation bubbles in the absence of external forcing are studied by means of linear stability analysis and direct numerical simulation. Previous studies demonstrated the existence of a three-dimensional modal instability, that becomes active for bubbles with peak reversed flow of approximately 7% of the free-stream velocity, well below the $\approx 16\%$ required for the absolute instability of Kelvin–Helmholtz waves. Direct numerical simulations are used to describe the nonlinear evolution of the primary instability, which is found to correspond to a supercritical pitchfork bifurcation and results in fully three-dimensional flows with spanwise inhomogeneity of finite amplitude. An extension of the classic weakly non-parallel analysis is then applied to the bifurcated flows, that have a strong dependence on the cross-stream planes and a mild dependence on the streamwise direction. The spanwise distortion of the separated flow induced by the primary instability is found to strongly destabilize the Kelvin–Helmholtz waves, leading to their absolute instability and the appearance of a global oscillator-type instability. This sequence of instabilities triggers the laminar–turbulent transition without requiring external disturbances or actuation. The characteristic frequency and streamwise and spanwise wavelengths of the self-excited instability are in good agreement with those reported for low-turbulence wind-tunnel experiments without explicit forcing. This indicates that the inherent dynamics described by the self-excited instability can also be relevant when external disturbances are present.

Key words: boundary layer stability, absolute/convective instability, transition to turbulence

1. Introduction

Laminar flow separation is typically associated with detrimental effects on the aerodynamics of lifting surfaces operating at relatively low Reynolds numbers. One kind of separated flow of particular applied interest is the laminar separation bubble (LSB) that forms near the leading edge of thin airfoils as the angle of attack is increased (Jones 1934). Separation of the laminar boundary layer takes place downstream of the suction peak on the airfoil lee side due to the adverse pressure gradient. The resulting separated

† Email address for correspondence: daniel.rodriguez@upm.es

shear layer encloses a region of slowly moving recirculating flow known as the dead-air region. Hydrodynamic instability dominates the dynamics of the separated layer, strongly amplifying external disturbances and leading to laminar–turbulent transition even at very low free-stream turbulence levels.

Leading-edge LSBs are classified as ‘short’ or ‘long’ based on their extent on the streamwise direction, and have distinctly different impacts on the aerodynamics (McCullough & Gault 1951). Short bubbles are characterized by a narrow plateau in the pressure distribution, which produces a small variation on the global forces acting on the airfoil. After small variations in the angle of attack or Reynolds number, a short bubble may fail to reattach within a short distance from separation, giving rise to a long bubble that extends over a substantial portion of the airfoil chord and affects substantially the aerodynamic forces. This phenomenon is referred to as bursting; its physical causes and the determination of an adequate criterion for its prediction are still today an active topic of research (Gaster 1967; Pauley, Moin & Reynolds 1990; Diwan, Chetan & Ramesh 2006; Marxen & Henningson 2011; Serna & Lázaro 2015; Mitra & Ramesh 2019, to cite a few).

The prevalence of flow instability in the separated shear layer suggests that a deeper understanding of the instability mechanisms acting on LSBs is of crucial importance in predicting and controlling the properties of separated flow and their impact on the aerodynamics of near-stall and stalled airfoils. This has motivated continued research on the instability of LSBs, both in airfoils and in simplified geometries. In particular, different models of separation bubbles on flat-plate boundary layers have been employed in which a deceleration or pressure gradient on the external flow field are prescribed. Kelvin–Helmholtz instability has been documented in a multitude of experimental (Dovgal, Kozlov & Michalke 1994; Diwan & Ramesh 2009; Michelis, Yarusevych & Kotsonis 2017) and numerical (Rist & Maucher 1994; Rist & Augustin 2006; Marxen, Lang & Rist 2012) investigations. Advected disturbance waves, generated by different receptivity mechanisms in the attached boundary layer, experience growths of several orders of magnitude when they reach the separated region, eventually leading to nonlinear effects and vortex shedding. Then, nonlinear interactions between the spanwise-dominant vortical structures lead to three-dimensionality and a very abrupt transition to turbulence (Alam & Sandham 2000; Rist & Augustin 2006; Jones, Sandberg & Sandham 2008; Marxen, Lang & Rist 2013; Robinet 2013). Alternatively, instability mechanisms generating streamwise-aligned structures stemming from incoming free-stream turbulence have also been identified (Marxen *et al.* 2009; Balzer & Fasel 2016; Hosseinverdi & Fasel 2018, 2019). These streamwise structures can interact with the Kelvin–Helmholtz rollers to produce different transition scenarios. For high turbulence intensity levels, the streamwise structures formed can even prevent the formation of spanwise-dominant vortices (Balzer & Fasel 2016; Hosseinverdi & Fasel 2019).

However, the description of laminar separation bubbles as mere amplifiers of external disturbances does not suffice to provide a comprehensive explanation of the wide variety of phenomena observed in these flows. One such phenomenon is the occurrence of flapping, i.e. a nearly periodic growth and reduction of the reversed flow region, which occurs in frequencies that are one order of magnitude lower than those typical of the inflectional instability (Zaman, McKinzie & Rumsey 1989). Another notable phenomenon is the appearance of stationary three-dimensional patterns in experiments (Bippes & Turk 1980; Diwan & Ramesh 2009; Passaggia, Leweke & Ehrenstein 2012; Kurelek, Lambert & Yarusevych 2016; Michelis, Yarusevych & Kotsonis 2018). A more fundamental aspect that is not explained is the onset of unsteadiness and three-dimensionality observed in direct numerical simulations of nominally two-dimensional LSBs in the absence of free-stream turbulence or external forcing (e.g. Spalart & Strelets 2000;

Hosseini-verdi & Fasel 2013; Balzer & Fasel 2016). Finally, the successful criteria proposed for the prediction of bursting, based on the assumption that it is entirely governed by quantitative changes of the convective inflectional instability, rely on experimental calibration (Gaster 1967; Diwan *et al.* 2006; Marxen & Henningson 2011; Serna & Lázaro 2015; Mitra & Ramesh 2019). This could be an indication that more involved instability processes are at the origin of bursting, as was postulated by some authors (Gaster 1963; Pauley *et al.* 1990; Diwan 2009).

This paper addresses the instability of LSBs in the absence of disturbances imposed externally and the series of flow bifurcations that transform an idealized steady, two-dimensional separated flow into an unsteady and three-dimensional transitional recirculation bubble. The exclusion of external disturbances precludes the amplifier behaviour, and only inherent (i.e. self-excited) flow instabilities can initiate the transition process. Herein, inherent dynamics not only refers to that corresponding to ideal, unforced LSBs, but also to that which may exist in practical externally disturbed flow, underlying the dominant inflectional instability and yet having an impact on the evolution and amplification of the external disturbances (e.g. Marquillie & Ehrenstein 2003; Rodríguez & Gennaro 2019).

The self-excited instability of LSBs has been addressed in the past by means of direct numerical simulations (Pauley *et al.* 1990; Fasel & Postl 2004; Embacher & Fasel 2014) and linear stability analyses (Allen & Riley 1995; Hammond & Redekopp 1998; Rist & Maucher 2002), under the assumption that such a self-excited mechanism is originated by spatial regions of absolute instability. A global oscillator, as described by Huerre & Monkewitz (1990), can then exist, leading to synchronized oscillations across the LSB and eventually initiating the self-sustained shedding of spanwise vortices. The subsequent secondary instabilities of the vortices would then result in three-dimensionality and transition to turbulence, closely resembling the scenario where external disturbance waves are continuously excited, making them difficult to be discerned. In order to quantify the intensity of the separation bubbles, and to serve as a criterion for the prediction of absolute instability, the peak reversed flow within the separation bubble scaled with the free-stream velocity (u_{rev}) has been widely used in the literature. Alam & Sandham (2000), Rist & Maucher (2002) and Diwan (2009) proposed threshold values $u_{rev} \approx 16\%–20\%$ for the onset of absolute instability, while the numerical simulations of Fasel & Postl (2004) and Embacher & Fasel (2014) reported a value $u_{rev} \approx 25\%$. Avanci, Rodríguez & Alves (2019) suggested that the occurrence of absolutely unstable Kelvin–Helmholtz waves in separated boundary-layer velocity profiles requires that the inflection point is located within the recirculating flow region and not necessarily a threshold on the reversed flow. They showed that absolutely unstable velocity profiles can be found for reversed flows lower than 16%. In this context, it is intriguing that the numerical simulations of Spalart & Strelets (2000) and Hosseini-verdi & Fasel (2013), which recovered transitional separation bubbles in the absence of continuous external disturbances, presented mean peak reversed flows below 8%.

Alternative self-excited instability mechanisms have been proposed, that consider the global nature of the LSB flow. An acoustic feedback cycle can exist in LSBs on airfoils, in which the passage near the trailing edge of vortical structures resulting from the convective amplification within the separated boundary layer produce acoustic emissions that excite new instability waves (Arbey & Bataille 1983; Nash, Lawson & McAlpine 1999; Jones *et al.* 2008). However, the absence of a trailing edge in the vicinity of the reattachment region rules out this instability for flat-plate geometries, like the one considered in the present study. Different global mechanisms were proposed by

Dallmann & Schewe (1987) and Gaster (2004), but their rigorous exploration was delayed by the success of the local instability analysis in describing the Kelvin–Helmholtz mechanism and its apparent ubiquity in experiments and simulations. It was not until Theofilis, Hein & Dallmann (2000) that an approach considering global eigenmodes was applied to a laminar separation bubble. A three-dimensional, temporally amplified eigenmode was identified, confirming the global instability mechanism suggested by Dallmann & Schewe (1987) a decade before. This instability, of a centrifugal nature, is present in two-dimensional flows featuring closed regions of recirculation, and has also been demonstrated for backward-facing steps (Barkley, Gomes & Henderson 2002; Beaudoin *et al.* 2004), lid-driven cavities (Albensoeder, Kuhlmann & Rath 2001; Theofilis, Duck & Owen 2004), open cavities (Brès & Colonius 2008; de Vicente *et al.* 2014), S-shaped ducts (Marquet *et al.* 2009), shock-wave boundary-layer interaction (Robinet 2007), stalled airfoils at very low Reynolds numbers (Kitsios *et al.* 2009; Rodríguez & Theofilis 2010a; Zhang & Samtaney 2016) and laminar separation bubbles past bumps (Gallaire, Marquillie & Ehrenstein 2007), to cite a few.

The application of the global eigenmode analysis to laminar separation bubbles has also contributed to shed new light on the physics stemming from the inflectional instability. Ehrenstein & Gallaire (2008) and Cherubini, Robinet & de Palma (2010a) suggested that the low-frequency flapping is originated by the linear superposition of a small number of unstable two-dimensional eigenmodes associated with absolutely unstable Kelvin–Helmholtz waves. The predicted flapping frequency was found to be in good agreement with the experiments of Passaggia *et al.* (2012). In a different vein, Alizard, Cherubini & Robinet (2009) applied a frequency-domain optimal response analysis based on globally stable two-dimensional eigenmodes to the study of external disturbances amplified by the LSB. The frequency corresponding to the optimal response in their analyses is in good agreement with that of the vortex shedding recovered in two-dimensional numerical simulations (Pauley *et al.* 1990).

With the aim of clarifying the relevance of the two self-excited instability mechanisms of LSBs on flat-plate boundary layers described so far, Rodríguez, Gennaro & Juniper (2013b) studied the two types of instability for a series of model LSBs. The three-dimensional eigenmode was found to become unstable for two-dimensional bubbles with peak reversed flow $u_{rev} \sim 6\%–8\%$, substantially lower than the threshold of 16% for the absolute instability. This finding suggests that, if disturbances of external origin are suppressed or reduced to very small amplitudes, the nominally two-dimensional separation bubbles would become three-dimensional prior to the onset of periodic oscillations or vortex shedding. The nature of this three-dimensionalization, a consequence of the structural instability of the two-dimensional flow (Dallmann & Schewe 1987), was investigated in Rodríguez & Theofilis (2010b) by means of topology reconstructions of the perturbed flow. The instability was found to produce a spanwise-periodic modulation of the recirculation bubble, giving rise to cellular separation patterns reminiscent of the U-shaped separation topologies defined theoretically by Hornung & Perry (1984), and also of the experimental observations of Bippes & Turk (1980) and Diwan & Ramesh (2009).

The objective of the present work is to show that three-dimensionalization of the LSBs induced by the primary self-excited instability can give rise to a self-excited secondary instability, explaining the origin of unsteadiness and triggering the transition to turbulence in the absence of external disturbances. Some quantitative features of the resulting transitional separation bubbles are in good agreement with those reported for quiet wind-tunnel experiments conducted without explicit forcing (Watmuff 1999; Serna & Lázaro 2014, 2015; Kurelek *et al.* 2016; Michelis *et al.* 2018).

1.1. Scope and outline

The flow configuration in Rodríguez & Theofilis (2010*b*) and Rodríguez *et al.* (2013*b*) is revisited here. A flat-plate boundary layer subjected to external flow deceleration is used for the construction of a family of steady and two-dimensional baseline LSBs. The linear analyses by Rodríguez *et al.* (2013*b*) serve as the departure point of the present research. The first objective of this work is to study the nonlinear evolution following the onset of the three-dimensional instability. A supercritical pitchfork bifurcation is found to be associated with it; the disturbance growth saturates for finite amplitudes leading to steady, fully three-dimensional separation bubbles. The secondary instability analysis of the bifurcated flows is the second objective of this paper.

The choice of an adequate methodology for the identification, isolation and analysis of different processes involved in the bifurcation sequence is not straightforward and has limited the analysis of three-dimensional separated states in the past. Direct numerical simulations, while recovering the complete flow evolution with remarkable fidelity, do not allow for the isolation of the individual instability mechanisms and can lead to misinterpretations of the bifurcation sequence. On the other hand, linear instability analyses based on the solution of eigenvalue problems are conditioned by the dimensionality of the underlying base flow, that has a tremendous impact on the computational expense associated with their numerical solution. In the present investigation, the three-dimensionality of the bifurcated flows would require a three-dimensional eigenmode problem for the secondary instability analysis. The first computations of three-dimensional linear instability eigenmodes (also referred to as tri-global instability analysis, Theofilis 2011) in the literature, either employing matrix-free (Tezuka & Suzuki 2006; Bagheri *et al.* 2009; Feldman & Gelfgat 2010; Loiseau *et al.* 2014) or matrix-forming (Gómez *et al.* 2012; Rodríguez & Gennaro 2017) approaches, are relatively recent and still limited by the availability of computational resources. An alternative methodology is used here for the analysis of three-dimensional flows in which the streamwise variations take place on a scale which is large compared to that of the cross-stream plane (Rodríguez & Gennaro 2015; Siconolfi *et al.* 2017), without simplifying assumptions on the in-plane shape of the disturbances. This is a natural extension of the classic weakly non-parallel approach that gave rise to the description of linear global oscillators (Chomaz, Huerre & Redekopp 1988; Huerre & Monkewitz 1990), but considering local (two-dimensional) cross-planes instead of (one-dimensional) velocity profiles.

The remainder of the paper is organized as follows. Section 2 presents the construction of the baseline LSBs. Section 3 describes the theoretical and numerical approaches used in the linear and nonlinear instability analyses. The primary instability is revisited in § 4, which also addresses the nonlinear evolution by means of direct numerical simulations. The secondary instability of the bifurcated LSBs is addressed in § 5. Section 6 illustrates the nonlinear evolution of the secondary instability and the transition to turbulence. Finally, the conclusions of this research and their relation with other works in the literature are discussed in § 7.

2. Model laminar separation bubbles

An inverse formulation of the non-similar incompressible boundary-layer equations is used to compute a family of baseline laminar separation bubbles. The computed flows are two-dimensional and steady by construction, and the emergence of three-dimensionalization or unsteadiness is to be recovered as flow instabilities.

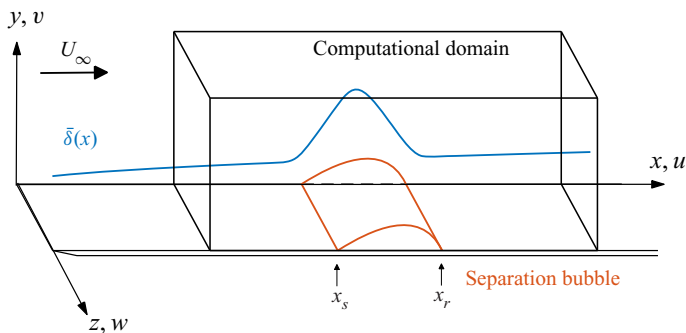


FIGURE 1. Problem geometry and computational domain.

2.1. Inverse formulation of the non-similar boundary-layer problem

Figure 1 illustrates the geometry of the model problem. The dimensional streamwise, wall-normal and spanwise coordinates are denoted by x^* , y^* and z^* , and their respective velocity components by u^* , v^* and w^* . Dimensionless magnitudes, to be defined later, follow the same nomenclature but the superscript $*$ is dropped. The boundary-layer edge velocity U_e^* and the kinematic viscosity ν^* are used to define the boundary-layer coordinates $\xi = x^*/L^*$ and $\eta = y^*\sqrt{U_e^*/\nu^*x^*}$, and the transformed streamfunction

$$f(\xi, \eta) = \Psi^*/\sqrt{U_e^*\nu^*x^*}. \quad (2.1)$$

The dimensional streamfunction is denoted by Ψ^* and L^* is an arbitrary scale length. After substitution of these variables in the streamwise momentum equation, the following equation for $f(\xi, \eta)$ is obtained:

$$f_{\eta\eta\eta} + \frac{m+1}{2}ff_{\eta\eta} + m(1-f_\eta^2) = \xi(\Theta f_{\eta\xi} + f_{\eta\xi}). \quad (2.2)$$

Subscripts denote partial differentiation, and $m = (\xi/U_e^*)(dU_e^*/d\xi)$ quantifies the free-stream pressure gradient, which only depends on ξ (Schlichting 1979). In order to recover separated states, the so-called FLARE approximation (Reyhner & Flüge-Lotz 1968; Carter 1975) is invoked, that neglects the streamwise convective term when reversed flow exists. The FLARE approximation appears in this equation as the function $\Theta(\xi, \eta)$, which takes value unity when $f_\eta \geq 0$ and vanishes if $f_\eta < 0$. Equation (2.2) is complemented with the boundary conditions

$$f(\xi, 0) = 0, \quad f_\eta(\xi, 0) = 0, \quad \text{and} \quad f_\eta(\xi, \eta \rightarrow \infty) \rightarrow 1. \quad (2.3a-c)$$

The direct formulation of the non-similar boundary-layer equations prescribes a distribution of the boundary-layer edge velocity $U_e^*(\xi)$ or the external-flow pressure gradient $m(\xi)$. However, this approach fails when a point of vanishing wall shear is reached, a phenomenon that is known as Goldstein's singularity (Howarth 1934). An inverse formulation is used here to circumvent the singularity; the displacement thickness distribution $\bar{\delta}(\xi)$ is imposed as the missing boundary condition

$$f(\xi, \eta \rightarrow \infty) \rightarrow 1 - \bar{\delta}(\xi). \quad (2.4)$$

The solution algorithm marches downstream and iterates on each ξ profile until a converged solution profile $f(\xi, \eta)$ and $m(\xi)$ are obtained. The inverse-problem

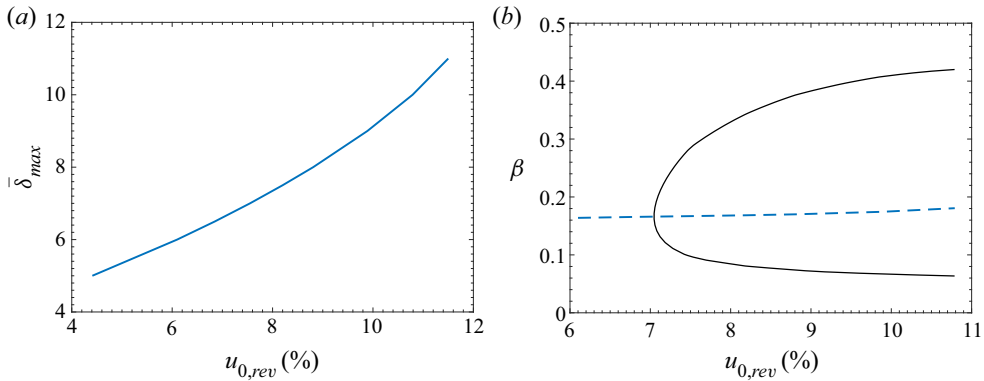


FIGURE 2. (a) Dependence of the peak reversed flow in the baseline LSB, $u_{0,rev}$, with the maximum displacement thickness, $\bar{\delta}_{max}$. (b) Neutral curve for the primary instability eigenmode (solid line) and spanwise wavenumber of maximum growth rate (dashed line).

formulation recovers the boundary-layer edge velocity $U_e^*(\xi)$ corresponding to the imposed displacement thickness distribution $\bar{\delta}(\xi)$, accounting for the viscous–inviscid interaction effects that cause Goldstein’s singularity. Details on the numerical solution can be found in Rodríguez (2010).

2.2. Construction of the baseline laminar separation bubbles

An analytical displacement thickness distribution analogous to that prescribed by Carter (1975) is imposed in (2.4). The solution of (2.2) is initiated with the velocity profile and $\bar{\delta}$ value corresponding to the Blasius solution ($\bar{\delta}_B = 1.72078$). The displacement thickness is increased over a finite extent along the streamwise direction, following an analytical expression that can be found in Rodríguez & Theofilis (2010*b*).

In what follows, lengths and velocities are scaled respectively with the displacement thickness δ_m^* and the free-stream velocity U_{in}^* at a streamwise location upstream of the increase of $\bar{\delta}$. This location is chosen so that the Reynolds number based on the local displacement thickness is $Re = 450$, which is comparable with that in reported direct numerical simulations (Rist & Maucher 1994; Alam & Sandham 2000; Spalart & Strelets 2000). Setting the arbitrary length $L^* = \delta_m^*$ leads to $\xi = x$. The increase of the displacement thickness over the Blasius value starts at a coordinate x_1 and returns to the Blasius value at x_2 . In boundary-layer coordinates, the function $\bar{\delta}(x)$ is symmetric about the coordinate $x_s = (x_1 + x_2)/2$, where it reaches its peak value, $\bar{\delta}_{max}$. Thus, $\bar{\delta}(x)$ is completely defined by the parameters x_1 , x_2 and $\bar{\delta}_{max}$. While $\bar{\delta}$ is symmetric, the resulting recirculation bubble is highly asymmetric and the locations of the peak negative wall shear and streamwise velocity are displaced towards the reattachment point. Prescribing an increase in the displacement thickness over the Blasius value is equivalent to imposing an adverse pressure gradient or a deceleration of the free stream, and these terms will be employed indistinctly in the rest of the paper.

Using the same approach, Rodríguez *et al.* (2013*b*) computed a series of baseline separation bubbles considering three different extents of the free-stream deceleration. For each extent, the value $\bar{\delta}_{max}$ was varied from 3 to 10 to generate a large number of different LSBs. In the present work, we consider only the family of model bubbles corresponding to the longest streamwise extent, defined by $x_1 = 210$, $x_2 = 320$ and varying $\bar{\delta}_{max}$.

The baseline two-dimensional LSBs in this study are constructed to be quantitatively comparable with other separation bubbles in the literature. Three magnitudes are computed for comparison: (i) the Reynolds number based on the momentum thickness and edge velocity at separation $Re_{\theta,s} = \theta_s^* U_{e,s}^* / \nu^*$, which lies in the range 208–212; the Reynolds number based on the length of the recirculation region and free-stream velocity $Re_L = (x_r^* - x_s^*) U_{in}^* / \nu^*$ (where x_r^* and x_s^* are the dimensional reattachment and separation locations), which is between 37 600 and 40 500; and (iii) the peak reversed flow scaled with the free-stream velocity, $u_{rev} = -\min(u^*) / U_{in}^*$. Figure 2(a) shows the variation of the peak reversed flow in the baseline LSBs, $u_{0,rev}$ with $\bar{\delta}_{max}$ (subscript 0 is used to denote the flow fields corresponding to the baseline LSBs). The maximum reversed flow that can be obtained with the boundary-layer formulation is $u_{0,rev} \approx 12\%$. This value corresponds to the peak reversed flow attainable in Falkner–Skan profiles, which are asymptotic solutions of the present formulation (Schlichting 1979).

3. Methodology

3.1. Modal linear instability analyses

Three-dimensional flows of viscous incompressible fluids are described by the continuity and Navier–Stokes equations

$$\nabla \cdot \mathbf{v} = 0, \quad \frac{\partial \mathbf{v}}{\partial t} + \mathbf{v} \cdot \nabla \mathbf{v} = -\nabla p + \frac{1}{Re} \nabla^2 \mathbf{v}, \tag{3.1a,b}$$

where $\mathbf{v} = (u, v, w)$ is the velocity field, p is the reduced pressure and Re is the Reynolds number, as defined in § 2.

Let $\mathbf{q} = (\mathbf{v}, p)$ be the total flow field. Linear stability theory studies the evolution of infinitesimally small disturbances \mathbf{q}' superimposed to a base flow $\bar{\mathbf{q}}$. The total flow field is decomposed as

$$\mathbf{q}(x, y, z, t) = \bar{\mathbf{q}}(x, y, z) + \epsilon \mathbf{q}'(x, y, z, t), \tag{3.2}$$

where $\epsilon \ll 1$. Substitution of (3.2) on the Navier–Stokes equations and linearization about the steady base flow results on the linearized Navier–Stokes equations, that can be recast in matrix form as

$$\mathbf{B} \frac{\partial \mathbf{q}'}{\partial t} = \mathbf{A}_{3D} \mathbf{q}'. \tag{3.3}$$

The linear operators \mathbf{A}_{3D} and \mathbf{B} depend on the base flow components and their spatial derivatives and on the Reynolds number, but not on time. This allows for the introduction of the modal form

$$\mathbf{q}'(x, y, z, t) = \hat{\mathbf{q}}(x, y, z) \exp(-i\omega t) + \text{c.c.}, \tag{3.4}$$

with c.c. denoting the complex conjugate, which results in the generalized eigenvalue problem (EVP)

$$-i\omega \mathbf{B} \hat{\mathbf{q}}(x, y, z) = \mathbf{A}_{3D}(\bar{\mathbf{q}}(x, y, z), Re) \hat{\mathbf{q}}(x, y, z), \tag{3.5}$$

where ω are the eigenvalues and $\hat{\mathbf{q}}$ the eigenfunctions.

The real part of the eigenvalues ω_r corresponds to a circular frequency of oscillation while the imaginary part ω_i is the growth rate. If all the eigenmodes have $\omega_i < 0$, then any disturbance introduced in the flow decays asymptotically for long times and the base flow is said to be linearly stable. Conversely, if $\omega_i > 0$ for at least one eigenmode, the base flow is unstable and the flow field evolves towards a different state.

In the most general case, when the base flow depends explicitly on the three spatial directions, so do the linear operators and the eigenfunctions; this EVP is known as three-dimensional eigenmode analysis or tri-global analysis (Theofilis 2011). Many problems of interest exist in which the base flow depends only on one or two spatial directions, enabling the introduction of Fourier modes on these directions and reducing substantially the complexity of the problem. Two such simplifications are relevant to the present work.

3.1.1. *Three-dimensional global eigenmodes of a two-dimensional non-parallel flow*

In the analysis of the primary instability to be discussed in § 4, the base flow corresponds to the baseline two-dimensional LSBs q_0 (described in § 2), which are homogeneous on the spanwise direction z . Spanwise-periodic eigenmodes are then introduced, of the form

$$q'(x, y, z, t) \sim \hat{q}(x, y) \exp[i(\beta z - \omega t)] + \text{c.c.}, \tag{3.6}$$

where β is a wavenumber associated with the spanwise periodicity length $\lambda_z = 2\pi/\beta$. This modal form simplifies the EVP to a two-dimensional one, identical to the one solved by e.g. Theofilis *et al.* (2000) or Barkley *et al.* (2002)

$$-i\omega \mathbf{B} \hat{q}(x, y) = \mathbf{A}_{2Dz}(\bar{q}(x, y), \beta, Re) \hat{q}(x, y). \tag{3.7}$$

The linear operator \mathbf{A}_{2Dz} is obtained from \mathbf{A}_{3D} by imposing a base flow of the form $\bar{q}(x, y)$ with $\bar{w} = 0$, and modal disturbances of the form (3.6). The resulting EVP must be complemented with adequate homogeneous boundary conditions, that will be discussed in § 4.

3.1.2. *Global oscillator analysis based on cross-stream planes*

A different simplification is used in § 5, in which the base flow corresponds to steady three-dimensional separation bubbles. A weakly non-parallel approximation is introduced, based on the assumption that the spatial scale L on which streamwise variations of the base flow are significant is large compared to those on the cross-stream section and to the instability wavelengths $\lambda_x = 2\pi/\alpha_r$. Evidence has been amassed that this approximation is valid for instability waves developing over laminar separation bubbles (Dovgal *et al.* 1994; Rist & Maucher 2002; Diwan & Ramesh 2012). Local instability analyses based on the weakly non-parallel approximation can be used to study the existence of self-excited instabilities consisting of synchronized oscillations across the flow field. When such an oscillator-type instability is present, weakly non-parallel analysis delivers results analogous to the more expensive global eigenmode computation (Pier 2002; Giannetti & Luchini 2007; Pier 2008; Juniper, Tammisola & Lundell 2011; Siconolfi *et al.* 2017). The weakly non-parallel analysis proposed by Chomaz *et al.* (1988) and Huerre & Monkewitz (1990), based on the Wentzel–Kramers–Brillouin–Jeffrey (WKBJ) approximation, is extended here to three-dimensional base flows which have a strong dependence on the two cross-stream directions. Only the main elements of the approach are described; a more detailed explanation can be found in Huerre & Monkewitz (1990) and Siconolfi *et al.* (2017).

The slow coordinate $X = \gamma x$ is defined, with $\gamma = \lambda_x/L$ assumed to be a small quantity. At each X -plane, the instability waves are locally described by the modal form

$$q'(x, y, z, t) \sim \hat{q}(X, y, z) \exp[i(\alpha(X)x - \omega t)] + \text{c.c.} \tag{3.8}$$

leading to a generalized EVP of the form

$$-i\omega \mathbf{B} \hat{q}(y, z) = \mathbf{A}_{2D_X}(\alpha, \bar{q}(X, y, z)) \hat{q}(y, z). \tag{3.9}$$

The linear operator \mathbf{A}_{2D_X} is obtained by substituting the disturbance form (3.8) in \mathbf{A}_{3D} . Following Siconolfi *et al.* (2017), terms proportional to first-order streamwise derivatives of the base flow quantities are retained. These additional $O(\gamma)$ terms have a small effect on the local stability properties of the flow, but their inclusion simplifies the numerical evaluation of the global frequency correction, described below.

In the analysis of local instability waves, both the streamwise wavenumber and the frequency can take complex values, i.e. $\omega = \omega_r + i\omega_i$ and $\alpha = \alpha_r + i\alpha_i$. The solution of this EVP delivers a complete eigenspectrum, from which only a small number of discrete eigenmodes correspond to potentially unstable waves. Successive solutions of (3.9) can be used to map the individual eigenmodes from the complex plane α to the complex plane ω at each X , establishing the dispersion relation $D(\alpha, \omega, X) = 0$. This dispersion relation governs the evolution of packets of disturbance waves (i.e. wavepackets) locally at the cross-stream plane X .

The analysis proceeds by determining, at each X -plane, the complex frequency associated with disturbance waves with zero group velocity $c_g = \partial\omega/\partial\alpha$. This frequency is known as the local absolute frequency $\omega_0(X)$, and the associated wavenumber is denoted by $\alpha_0(X)$. A temporally amplified absolute frequency ($\omega_{0,i} > 0$) implies instability waves that grow in amplitude while propagating upstream. The base flow is then said to be absolutely unstable locally at the X -plane, as opposed to convectively unstable conditions for which only downstream propagating waves grow in amplitude.

If the streamwise portion of the base flow being absolute unstable is sufficiently large, a self-exciting mechanism can exist leading to synchronized oscillations, characterized by the complex global oscillation frequency

$$\omega_g = \omega_s + \gamma\omega_\gamma. \tag{3.10}$$

The leading-order contribution ω_s is given by the saddle point of $\omega_0(X)$ on the complex X -plane, $d\omega_0/dX = 0$. The complex X coordinate that satisfies this condition is referred to as the wavemaker X_s and $\omega_s = \omega_0(X_s)$. The correction term ω_γ will be discussed shortly below.

The spatial structure of the oscillator is calculated by investigating how the flow responds to the saddle-point frequency, i.e. by evaluating

$$q'(x, y, z, t) \sim \Psi_0(X) \hat{q}^\pm(y, z; X, \omega_s) \exp\left(\frac{i}{\gamma} \int_X \alpha^\pm(X', \omega_s) dX' - i\omega_g t\right) + \text{c.c.} \tag{3.11}$$

The results of the local EVP are used at each X -plane: α^- and α^+ are respectively the upstream- and downstream-propagating local wavenumbers, which are considered at each side of the wavemaker X_s and satisfy (3.9) for $\omega = \omega_s$. Similarly, \hat{q}^\pm are the corresponding local eigenfunctions associated with α^\pm . The global oscillator structure is computed by integrating the α^- branch upstream of X_s and the α^+ downstream of X_s . The WKBJ approximation breaks down in a small region around the saddle point, for which a different scaling of the streamwise variables and disturbance form are required (Huerre & Monkewitz 1990). The asymptotic matching of the outer α^- and α^+ solutions and the

inner WKB solution determines the values admitted by the correction term ω_γ :

$$\omega_\gamma = -\frac{i}{2}\omega_{\alpha\alpha}\alpha_{0,X} + (\omega_{0,XX}\omega_{\alpha\alpha})^{1/2}(n + 1/2), \quad (3.12)$$

where $\omega_{\alpha\alpha} = \partial^2\omega/\partial\alpha^2$, $\alpha_{0,X} = \partial\alpha_0/\partial X$ and $\omega_{0,XX} = \partial^2\omega_0/\partial X^2$, all of them evaluated at the saddle point X_s . The non-negative integer n accounts for different matching solutions. The value $n = 0$ is chosen for all the computations in this paper, as it corresponds to the solution with a larger growth rate. The scalar function $\Psi_0(X)$ in (3.11) is determined from the matching of the inner and outer solutions. However, Juniper *et al.* (2011) showed that the error incurred in assuming a uniform value for Ψ_0 is smaller than the influence of the inaccuracies in α^\pm . Consequently, Ψ_0 is taken as uniform here too.

3.1.3. Numerical methods for instability analysis

The solution of the two- and three-dimensional EVPs is done using the code presented in Rodríguez & Gennaro (2017). Variable-stencil finite differences are used to discretize the linear operators. The stencil varies from centred 7-point finite differences in the inner points to forward or backward differences with 4 points at the boundaries. This discretization has the benefit of producing very sparse and banded matrix blocks, optimizing the sparse algebra efficiency while presenting an improved resolution over low-order discretization methods (Gennaro *et al.* 2013). A coordinate transformation is introduced to concentrate the computational mesh at the flat plate. In-house implementations of sparse storage and operation algorithms and a shift-and-invert Arnoldi algorithm are used. The multi-frontal sparse linear algebra MUMPS (Amestoy *et al.* 2001) is used for the lower-upper (LU) factorization of the sparse matrices and for performing the required substitutions. Matrix-line reordering is previously applied using the library METIS, and shared-memory parallelization is achieved by using OpenMP.

3.2. Direct numerical simulations

Direct numerical simulations (DNS) are performed to validate the results of the linear analyses and to study the nonlinear regimes. The main characteristics of the code employed are summarized here; the complete description of the methodology and validations can be found in Petri *et al.* (2015). The Navier–Stokes equations in the velocity–vorticity formulation are discretized using compact finite differences (Lele 1992). Fifth- and sixth-order formulas are used for the x and y directions, respectively. A coordinate transformation is applied to the y direction to increase the resolution towards the flat plate. Fourier modes are used in the spanwise direction, and the derivatives are computed via fast Fourier transform. The time derivatives in the vorticity transport equations are discretized using a fourth-order, four-step Runge–Kutta integration scheme. Time advancement requires the solution of a number of Poisson equations, which are solved using a multigrid full approximation scheme (Strüben & Trottenberg 1981) with a V-cycle with 4 overlapped grids. The coefficient matrices for the derivative calculation and for the Poisson equation solution suggested by Linnick & Fasel (2005) were used.

The disturbance formulation of the equations is used in the present simulations. The wall and far-field boundary conditions are consistent with those imposed in the stability analyses, to be discussed later. The multigrid solution of the Poisson equation requires vorticity to vanish at inflow and outflow boundaries, for which buffer layers are defined following Kloker & Konzelmann (1993).

3.2.1. Selective frequency damping

Selective frequency damping (SFD) consists in the addition of an explicit forcing term to the governing equations solved in the DNS, that acts as a frequency low-pass filter (Åkervik *et al.* 2006). This work uses SFD to isolate the nonlinear evolution associated with the primary bifurcation from the secondary instabilities that give rise to unsteadiness (§ 4.3). The encapsulated formulation of the SFD method proposed by Jordi, Cotter & Sherwin (2014) has been implemented in the DNS code. Details on the methodology can be found in the original reference.

4. Primary instability: steady three-dimensionalization

4.1. Recapitulation of the properties of the primary linear instability

The three-dimensional instability of the steady, two-dimensional baseline LSBs is analysed using a global eigenmode problem, in which modal perturbations of the form (3.6) are studied. Homogeneous Dirichlet boundary conditions are imposed at the inlet and far field, and no-slip conditions are imposed at the wall. Homogeneous Neumann boundary conditions are used at the outlet, but alternatives like linear extrapolation (Theofilis *et al.* 2000; Rodríguez & Theofilis 2010*b*) or no-stress conditions (Marquet *et al.* 2008) deliver consistent results.

Following this approach, Theofilis *et al.* (2000) showed the existence of a self-excited eigenmode, that has been recovered recurrently in the literature in flows with closed recirculation regions (e.g. Barkley *et al.* 2002; Gallaire *et al.* 2007; Marquet *et al.* 2008; Cherubini *et al.* 2010*b*; Rodríguez & Theofilis 2010*a*; Gennaro, Souza & Rodríguez 2019). Figure 2(*b*) shows the neutral curve corresponding to the baseline LSBs \mathbf{q}_0 . The computational domain used in the computations is $x \in [80, 750]$ and $y \in [0, 100]$, with resolution $N_x = 901$ and $N_y = 501$. This mesh is used to ensure the integrity of the results when interpolated in the DNS mesh (§ 4.2), but the convergence of the leading eigenmode is achieved with substantially smaller domain and resolution. In the figure, the peak reversed flow $u_{0,rev}$ is used to characterize the baseline LSB instead of δ_{max} . Three main characteristics define this instability: (i) the peak reversed flow required for the instability is well below the $u_{rev} \approx 15\%$ threshold generally admitted for the onset of absolute instability of two-dimensional disturbance waves; (ii) the dominance of a finite spanwise wavenumber β , rendering the instability three-dimensional; and (iii) the eigenmode is stationary for the range of dominant wavenumbers, $\omega_r = 0$. For the baseline separation bubbles analysed here, critical conditions occur at $\delta_{max,c} \approx 6.61$ (corresponding to $u_{0,rev} \approx 7\%$) and $\beta_c = 0.166$.

4.2. Set-up of direct numerical simulations

Direct numerical simulations are used to cross-validate the linear stability results (see appendix A) and study the nonlinear evolution of the disturbed flow on account of the self-excited modal instability. The disturbance form of the Navier–Stokes equations is used, with the baseline LSBs \mathbf{q}_0 as base flow. The fluctuation flow variables \mathbf{q}' are separated in spanwise Fourier modes

$$\mathbf{q}' = \sum_{k=0}^{N_k} \tilde{\mathbf{q}}_k(x, y, t) \exp(ik\beta z) + \text{c.c.}, \quad (4.1)$$

where N_k is the maximum number of Fourier modes allowed in the computation, and β is the fundamental wavenumber, taken as $\beta_c = 0.166$.

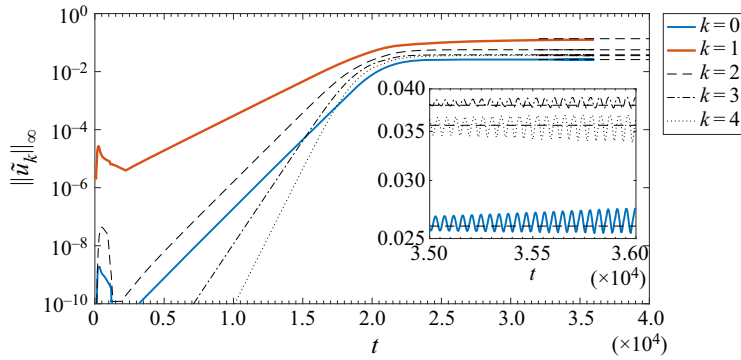


FIGURE 3. Temporal evolution of modal amplitudes. Baseline LSB corresponds to $\bar{\delta}_{max} = 8.5$, $u_{0,rev} = 9.37\%$. The inset shows the small-amplitude oscillations that develop towards the growth saturation of the primary instability. Horizontal lines correspond to the converged amplitudes after the SFD is activated.

The same computational domain as in the linear stability analysis is used. The time step is $\Delta t = 0.78$, the number of discretization points in the x and y directions used is $N_x = 401$ and $N_y = 241$ and the number of spanwise Fourier modes is $N_k = 64$. The wall-normal and spanwise resolutions are comparable to those by Marxen *et al.* (2013), while the streamwise resolution is lower. This resolution allows the accurate identification of the instability mechanisms that arise in the laminar base flow and does not intend to fully resolve the subsequent turbulent flow. For validation purposes, some of the simulations are repeated using the higher resolution $N_x \times N_y \times N_k = 1201 \times 241 \times 128$ and the time step $\Delta t = 0.78/8 = 0.0975$. These simulations are denoted as DNSh in what follows, and have excellent agreement with the lower resolution ones in what concerns this section, as shown in appendix A.

The simulations are initiated with the disturbance field corresponding to the leading global eigenmode alone; the Fourier mode \tilde{q}_1 is initiated with the unstable eigenfunction and $\tilde{q}_k = 0$ for $k \neq 1$. This includes $k = 0$, which corresponds to the spanwise-average flow distortion. The initial condition is scaled so that the peak spanwise velocity $\|\tilde{w}_1\|_\infty = 10^{-6}$, and the respective peak streamwise velocity $\|\tilde{u}_1\|_\infty \approx 2.57 \times 10^{-6}$.

4.3. Nonlinear evolution: supercritical pitchfork bifurcation

Figure 3 shows the temporal evolution of the first few Fourier modes for the representative baseline LSB defined by $\bar{\delta}_{max} = 8.5$, $u_{0,rev} = 9.37\%$. The small amplitude of the initial condition ensures that the flow undergoes an initial phase of linear evolution. The peak streamwise velocity of the corresponding Fourier mode is used to monitor the modal amplitudes. The initial transient ($t \leq 50$) is related to the adaptation of the initial condition to the outlet buffer layer used in the DNS.

The linear growth of the fundamental $k = 1$ mode gives rise to wavenumber harmonics and a spanwise-average flow distortion through nonlinear interactions. As the $k \neq 1$ modes reach amplitudes comparable to that of the fundamental mode, the growth dictated by the linear instability is reduced and eventually saturates. The result is a bifurcated state (with respect to the two-dimensional baseline LSB q_0) presenting a steady, three-dimensional laminar separation bubble. For baseline LSBs sufficiently close to the neutral conditions of the primary instability, this process can be studied by means of the weakly nonlinear

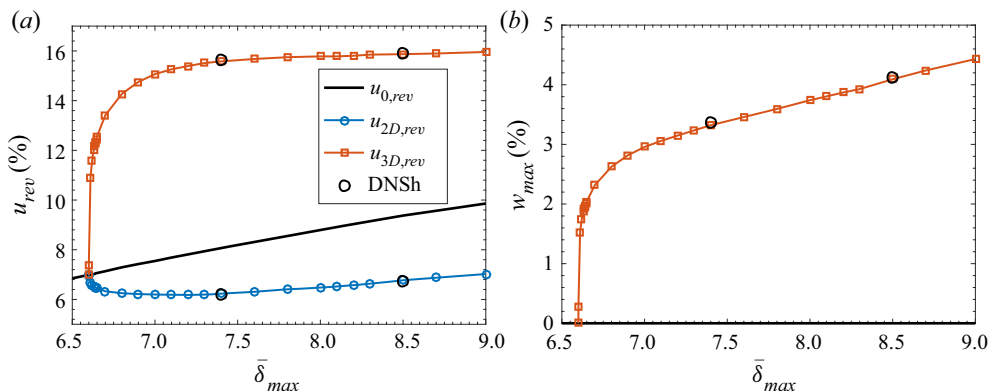


FIGURE 4. Bifurcation diagram of the primary instability, corresponding to the saturation of the three-dimensional instability. (a) Peak reversed flow of the baseline LSB ($u_{0,rev}$, solid line without symbols), the saturated three-dimensional flow ($u_{3D,rev}$, squares) and the spanwise-averaged saturated flow ($u_{2D,rev}$, circles). (b) Peak spanwise velocity (w_{max} , squares). Large circles correspond to the DNSh simulations.

stability theory, as done by Rodríguez & Gennaro (2015). The bifurcation is found to be a supercritical pitchfork one: two-dimensional LSBs with reversed flow below the critical value remain two-dimensional in the absence of external sustained excitation. Conversely, at supercritical conditions, the flow develops a three-dimensional distortion, whose amplitude at saturation is proportional to the departure from the critical conditions. The pitchfork bifurcation is better visualized by monitoring the peak spanwise velocity w_{max} at saturated conditions (figure 4).

If the numerical simulation is marched for a long enough time, oscillations of the amplitudes of the Fourier modes appear, as shown in the inset in figure 3. These oscillations are not observed for all cases, but only for LSBs with $u_{0,rev}$ beyond a certain value. It is anticipated here that they correspond to a self-excited secondary instability of the three-dimensional separated flows that will be addressed in § 5. When this happens, the spontaneous flow unsteadiness prevents the direct determination of the steady three-dimensional bifurcated flow corresponding to the saturation of the primary instability. In order to circumvent this and to isolate the saturation of the primary instability from the onset of the secondary instability, the SFD is used. Simulations are marched until the amplitudes of the first 6 Fourier modes are converged up to the eighth decimal case. Figure 4 shows the bifurcation of the peak reversed flow and peak spanwise velocity in the saturated flow. As a consequence of the spanwise-periodic distortion, the different spanwise planes have an increased or reduced reversed flow. The peak reversed flow $u_{rev,3D}$ at saturated conditions is found to increase drastically with respect to the baseline LSBs: e.g. $u_{rev,3D} \approx 15\%$ for $u_{0,rev} = 7.54\%$. The spanwise average of the bifurcated flow, obtained as the sum of the baseline LSB and the mean flow distortion mode ($q_{2D} = q_0 + \tilde{q}_0$), is also monitored. As opposed to $u_{3D,rev}$, the peak reversed flow in the spanwise-averaged flow $u_{2D,rev}$ is found to decrease with respect to the baseline LSB, presenting values between 6% and 7% for the range of parameters considered.

4.4. Features of the saturated three-dimensional flow field

Rodríguez & Theofilis (2010b) showed that the linear instability induces a spanwise-periodic modulation of the intensity and size of the recirculation region.

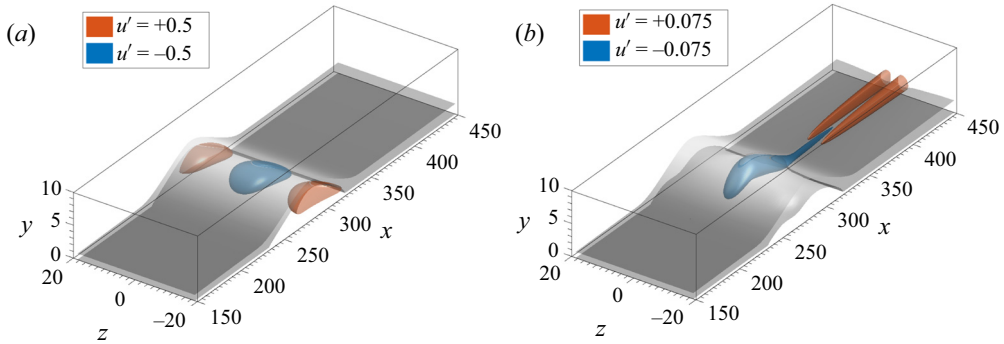


FIGURE 5. (a) Baseline LSB and eigenmode corresponding to the primary instability. Nearly horizontal grey surfaces correspond to $u_0 = 0.5$ and to the local zero-mass-flux coordinate y_d . The surfaces correspond to $u' = \pm 0.5$ of the eigenfunction streamwise velocity component. The eigenfunction is normalized with $\|u'\|_\infty = 1$. (b) Steady three-dimensional LSB resulting from the saturation of the primary instability. The horizontal grey surfaces correspond to $\bar{u}_{3D} = 0.5$ and to the local zero-mass flux coordinate y_d based on \bar{u}_{3D} . The baseline LSB corresponds to $\bar{\delta}_{max} = 7.4$, $u_{0,rev} = 8.06\%$.

The nonlinear effects leading to the saturation of the primary instability induce additional changes in the features of the three-dimensional separated flow. The representative case corresponding to $\bar{\delta}_{max} = 7.4$, $u_{0,rev} = 8.06\%$ is considered in the following discussion. Figure 5 shows three-dimensional flow fields corresponding to the linear eigenmode and to the saturated conditions. The plane $z = 0$ is arbitrarily chosen to coincide with the peak of negative velocity, and a complete spanwise period is shown. In all cases, two surfaces are shown to depict the separation bubble. The first surface is defined by the wall-normal coordinate $y_d(x, z)$ below which the mass flow rate in the streamwise direction is zero,

$$\int_0^{y_d} u(x, y, z) dy = 0. \quad (4.2)$$

In the limit of parallel flow, y_d corresponds to the location of the divisory streamline bounding the recirculating flow. The second surface is defined by $u = 0.5$. In the separated flow region, this surface approximates the location of the local inflection points y_i , where the spanwise vorticity $\omega_z \approx \partial u / \partial y$ is maximum. As will be discussed in § 5, these two surfaces are especially relevant for the secondary instability.

Figure 5(a) shows the streamwise velocity component u' corresponding to the primary instability linear eigenmode. Positive and negative disturbance velocities localized in the downstream part of the recirculation region are visible. Figure 5(b) shows the disturbance streamwise velocity field u' at the saturation conditions. The most prominent differences are: (i) the intensity of the negative peak is increased with respect to the positive peak in the recirculation region and (ii) two high-speed streaks are formed symmetrically downstream of the negative peak. The interpretation of (i) must be done carefully: figure 4(a) shows that the peak reversed flow in the bifurcated flow increases substantially compared to the baseline LSB, but the spanwise-average reversed flow is indeed reduced. This results in a localized pocket of very intense reversed flow centred on $z = 0$, while the rest of the separated flow becomes milder in terms of reversed flow. Similar streaky structures have been reported by Alam & Sandham (2000), Marxen & Henningson (2011) and Cherubini *et al.* (2010b) in direct numerical simulations and by Watmuff (1999) in experiments. A very similar picture is observed in the numerical simulations by

Pauley (1994) and Marxen *et al.* (2009), who relate them to Görtler vortices, and in those by Hosseinverdi & Fasel (2018) and Hosseinverdi & Fasel (2019), who identify them as Klebanoff modes. These structures appear here in the absence of free-stream disturbances, in a form which is incidentally consistent with the unforced simulations in Hosseinverdi & Fasel (2013) and Balzer & Fasel (2016).

5. Secondary instability: onset of unsteadiness

The previous section shows that the self-excited primary instability of LSBs corresponds to a supercritical bifurcation that leads to three-dimensional flow fields. This section analyses these bifurcated flows to ascertain if a secondary self-excited instability exists, as suggested by the oscillations appearing in [figure 3](#).

5.1. Cross-stream plane stability analysis of separated flows

The flow fields resulting from the saturation of the primary instability are taken as the base flow. These include the steady three-dimensional LSBs, denoted by \bar{q}_{3D} , and their spanwise average \bar{q}_{2D} . A classic one-dimensional analysis based on the Orr–Sommerfeld equation, that neglects the spanwise dependence of the base flow, would lead to important errors and cannot be applied here (see [appendix B](#)). Therefore, local stability analysis is applied to y – z cross-stream planes, as explained in § 3.1.2. The computational domain extends up to $y_{max} = 80$ in the wall-normal direction and one wavelength of the fundamental wavenumber in the spanwise direction ($\lambda_z = 2\pi/0.166 \approx 37.85$). No-slip boundary conditions are prescribed at the wall, and vanishing velocity and pressure are imposed at the far field. Periodicity is imposed on the spanwise direction. The cross-plane is discretized using $N_y = 71$ and $N_z = 60$ points. This resolution is enough to converge the leading discrete eigenvalues, relevant to the subsequent analysis, to a relative error in the fourth representative digit.

In order to illustrate the local instability properties of the cross-stream sections, the plane $X = 286$ corresponding to the baseline LSB with $\delta_{max} = 7.4$, $u_{0,rev} = 8.06\%$ is considered next. The complex streamwise wavenumber chosen, $\alpha = 0.42 - i0.33$, roughly approximates the α_0 in the absolute/convective analysis of the three-dimensional bifurcated flow \bar{q}_{3D} for this case (see [figure 8](#)). [Figure 6](#) shows the eigenvalue spectra corresponding to \bar{q}_{3D} and \bar{q}_{2D} . While a cheaper one-dimensional stability analysis could be applied to \bar{q}_{2D} on account of its spanwise homogeneity, the cross-stream analysis is also used to allow direct comparisons and facilitate the interpretation of the results for \bar{q}_{3D} . Both eigenspectra present the same structure, with a branch of stable eigenmodes starting at $\omega \approx 0 + i0$ and becoming gradually more stable as their frequency increases, and a family of discrete eigenmodes with $\omega_r \approx 0.13$ – 0.15 . The leading discrete eigenmodes are denoted as A , B and C .

Eigenmode A for \bar{q}_{2D} ([figure 6d](#)) presents the well-known features of a plane ($\beta = 0$) Kelvin–Helmholtz (K–H) wave on a boundary-layer profile with reversed flow, with the peak streamwise velocity located at the base flow inflection point (e.g. Dovgal *et al.* 1994). Eigenmodes B and C are overlapped in the eigenspectrum for \bar{q}_{2D} and correspond to the same oblique K–H wave with $\beta = \beta_c$ ([figure 6f,h](#)). This wavenumber is imposed here by the choice of the spanwise extent of the computational domain. The eigenfunctions for the two modes are phase shifted in the spanwise direction, presenting symmetric or antisymmetric velocity components about $z = 0$.

[Figure 6\(c,e,g\)](#) shows the eigenfunctions corresponding to eigenmodes A , B and C for the \bar{q}_{3D} base flow. The periodic spanwise distortion of the base flow leads to the ensuing modification of the K–H waves. The disturbance streamwise velocity is localized around

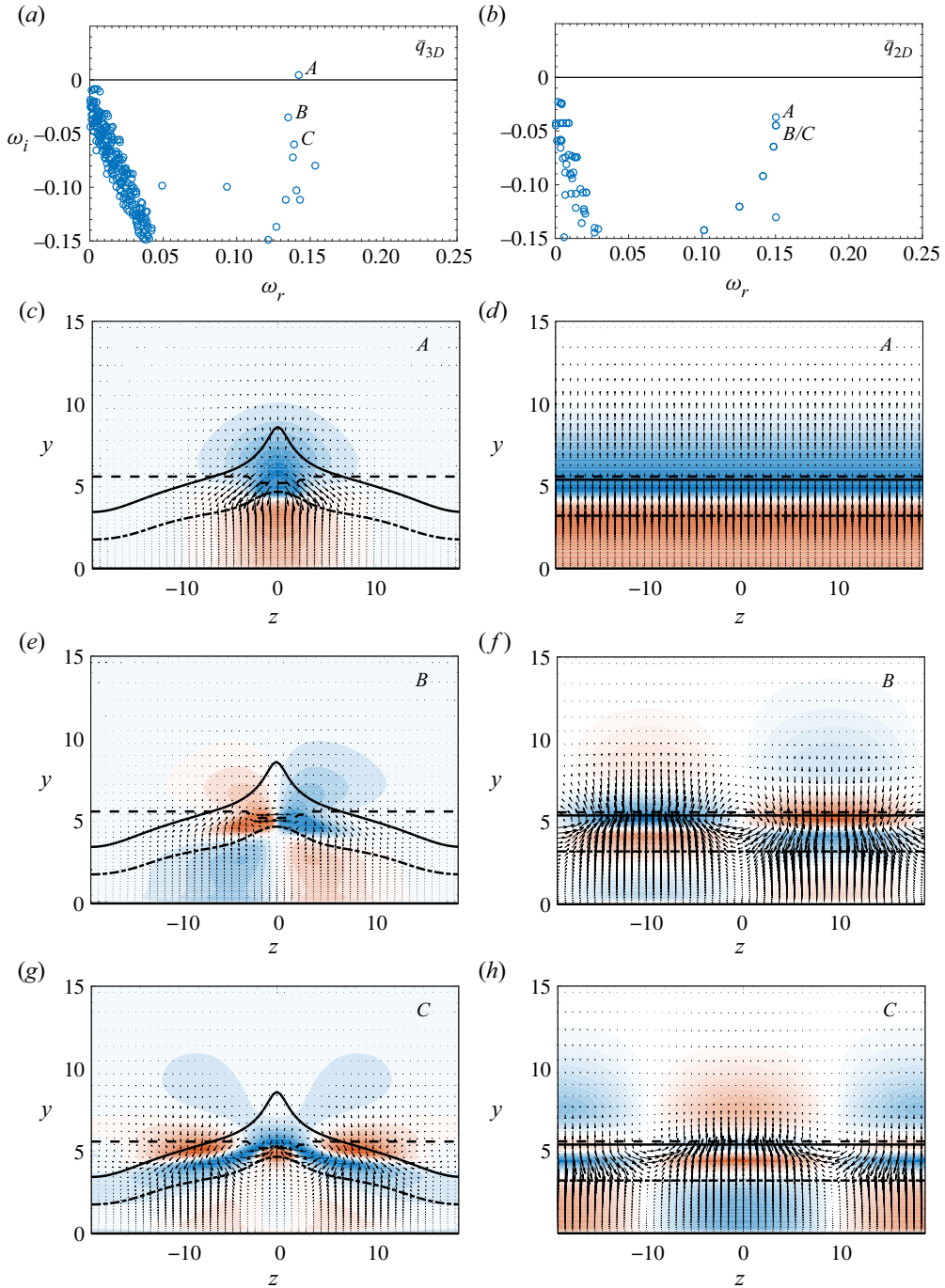


FIGURE 6. Linear stability analysis of the cross-stream plane $X = 286$ of \bar{q}_{3D} (a,c,e,g) and \bar{q}_{2D} (b,d,f,h) corresponding to the baseline LSB with $\bar{\delta}_{max} = 7.4$, $u_{0,rev} = 8.06\%$. The axial wavenumber is $\alpha = 0.42 - i0.33$. (a,b) Eigenvalue spectra. (c–h) Eigenfunctions corresponding to (c,d) eigenmode A, (e,f) eigenmode B, (g,h) eigenmode C. Contours correspond to streamwise velocity (perpendicular to figure) and the arrows to the velocities in the cross-plane. Contour levels are evenly spaced between $\pm \|\hat{u}\|_{\infty}$, with the zero level being white. The thick dashed-dotted, dashed and solid lines show the locations of the end of the reversed flow region (y_r), the streamwise inflection point (y_i) and the local divisory streamline (y_d), respectively.

the spanwise location of the peak reversed flow ($z = 0$). The symmetric or anti-symmetric characteristics and the number of phase changes on the $z = 0$ plane guide the identification of the corresponding eigenmodes in \bar{q}_{2D} and \bar{q}_{3D} . Eigenmode A, corresponding to the distorted plane K–H wave, is consistently found to be the most unstable or least stable in all the analyses done herein. The other eigenmodes are not considered further.

These results for separated boundary-layer profiles with spanwise distortion are consistent with inviscid analyses of spanwise-inhomogeneous shear layers (Saxena, Leibovich & Berkooz 1999; Kawahara *et al.* 2003; Marant & Cossu 2018). In these works, K–H instability waves that are symmetric (varicose) or antisymmetric (sinuous) about the crests of the shear layer are related to the formation of streamwise streaks, and the spanwise modulation of an unbounded shear layer is found to have a destabilizing effect. The presence of a solid wall close to the shear layer is found here to further promote the inflectional instability when spanwise distortion exists, as opposed to spanwise-homogeneous shear layers (Kawahara *et al.* 2003).

5.2. WKB analysis of the global oscillator

The absolute/convective instability of K–H waves and the existence of a global oscillator is addressed next. Following the procedure outlined in § 3.1.2, local analysis is applied to cross-stream planes separated $\Delta X \approx 1.67$ from each other. The dispersion relation $D(\alpha, \omega, X) = 0$ is obtained by mapping the complex α -plane to the ω -plane for each X cross-plane. The α -plane is discretized using a constant spacing $\Delta\alpha = 0.005$ both for the real and imaginary parts. The cusp-point method (Huerre & Monkewitz 1990; Schmid & Henningson 2001) is used to determine the absolute frequency ω_0 and the corresponding wavenumber α_0 at each X . Figures 7 and 8 show $\omega_0(X)$ and $\alpha_0(X)$ for the base flows \bar{q}_{2D} and \bar{q}_{3D} , respectively. In line with the analyses of the baseline LSB flows q_0 (Rodríguez, Gennaro & Juniper 2013a), the spanwise-average bifurcated flows \bar{q}_{2D} are found to be only convectively unstable. In contrast, the three-dimensional flows \bar{q}_{3D} present regions of absolute instability localized in the downstream part of the recirculation region. Absolute instability appears for $u_{0,rev} \geq 7.29\%$ ($\bar{\delta}_{max} \geq 7$). These base flows satisfy the necessary condition for the absolute instability of separated boundary-layer profiles proposed by Avanci *et al.* (2019), namely that the inflection point is located below the line of zero streamwise max flux $y_i < y_d$. This condition is visible in figure 6.

The existence of a region of absolute instability can lead to the appearance of a global oscillator. The application of the saddle-point condition $d\omega_0/dX = 0$ for the determination of the wavemaker X_s requires the analytical continuation of the dispersion relation to the complex X -plane. This is achieved here by fitting a polynomial to $\omega_0(X)$ and $\alpha_0(X)$, as described by Pier (2002). The indications given by Juniper & Pier (2015) (see also Siconolfi *et al.* 2017) to ensure the robust identification of X_s and ω_g are also followed. These validations are not described here for the sake of brevity.

Figure 9 shows the complex global frequency ω_g , the wavenumber α_g and the wavemaker location X_s as a function of the peak reversed flow of the baseline LSB, for the bifurcated three-dimensional flows \bar{q}_{3D} . The global oscillator becomes temporally amplified for $u_{0,rev}$ above $\approx 8.1\%$, ($\bar{\delta}_{max} \approx 7.5$). At these conditions, the peak reversed flow $u_{3D,rev} \approx 15.6\%$, while $u_{2D,rev} \approx 6.3\%$, and the spanwise-average flow \bar{q}_{2D} is globally (and absolutely) stable.

The spatial structure of the secondary instability global oscillator is shown in figure 10. The disturbance flow field is computed by evaluating (3.11) downstream of the wavemaker, using $\alpha^+(X)$ and $\hat{q}^+(y, z; X)$ only. Figure 10(a) shows the plane $z = 0$ corresponding to the peak reversed flow in the base flow \bar{q}_{3D} . The location of the local divisory streamline y_d ,

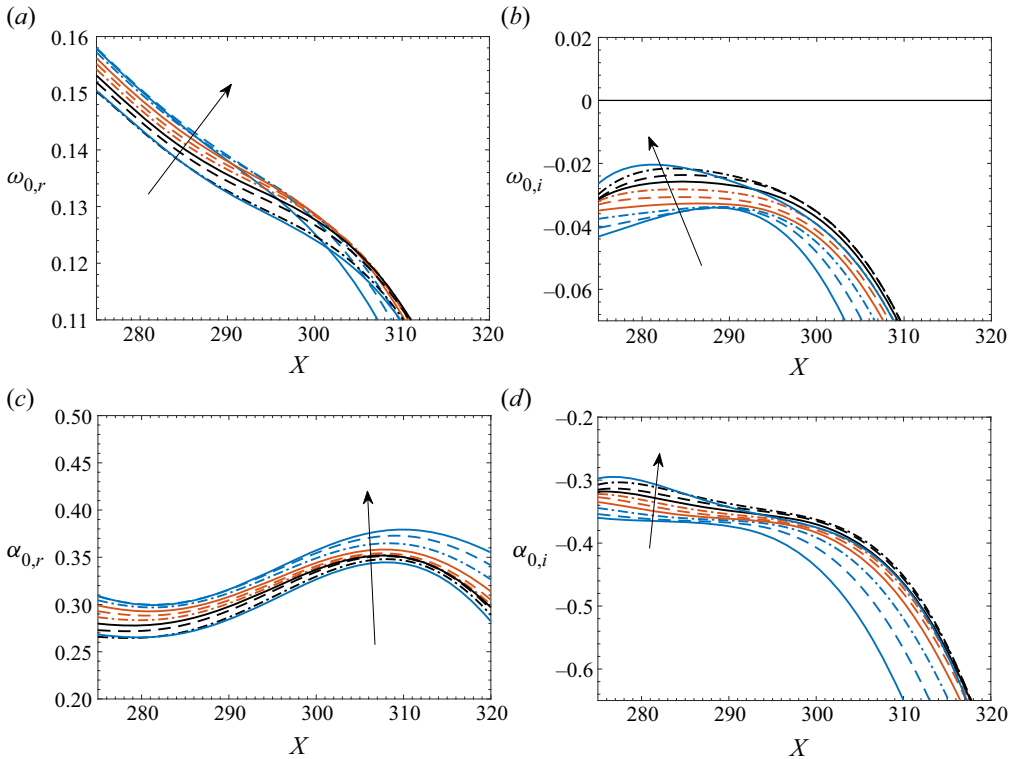


FIGURE 7. Absolute frequency and wavenumber of spanwise-averaged bubbles \bar{q}_{2D} . (a,b) Real and imaginary parts of the absolute frequency ω_0 . (c,d) Real and imaginary parts of the wavenumber α_0 . The lines correspond to (in the direction of the arrows): $\delta_{max} = 6.8, 7, 7.2, 7.4, 7.8, 8, 8.2, 8.5$ and 8.7 ; respectively $u_{0,rev} = 7.29\%, 7.54\%, 7.81\%, 8.06\%, 8.31\%, 8.56\%, 8.80\%, 9.04\%, 9.37\%$ and 9.57% .

$u = 0.5$ (which roughly approximates the location of the inflection point y_i in the separated flow region), and the zero streamwise velocity coordinate y_r are also shown. The contours of disturbance streamwise velocity are the typical ones of the K–H instability waves, peaking at the inflection point and tilted in the direction of the base flow shear. Figure 10(b) shows the plane $y = 1.75$, corresponding to approximately the $u = 0.5$ level downstream of reattachment. The spatial structure is found to be strongly dependent on the spanwise direction and localized symmetrically around the $z = 0$ plane.

5.3. Cross-validation of the secondary instability with direct numerical simulations

The steady base flows considered in the previous analyses of the secondary instability were computed using direct numerical simulations. Selective frequency damping (briefly described in § 3.2.1) was used to prevent the appearance of self-excited oscillations and isolate the nonlinear saturation of the primary instability from the eventual secondary instability. The solution was marched in time until the amplitudes of the first 6 spanwise Fourier modes were converged up to the eighth decimal case; the steady flows \bar{q}_{3D} were then considered to be converged. To cross-validate the results of the WKBJ analysis, the simulations are re-started from the instant (named t_0 , different for each baseline LSB) in which the steady flows \bar{q}_{3D} were established. The forcing term corresponding to the SFD is switched off abruptly at t_0 , introducing a small disturbance of the flow field which is

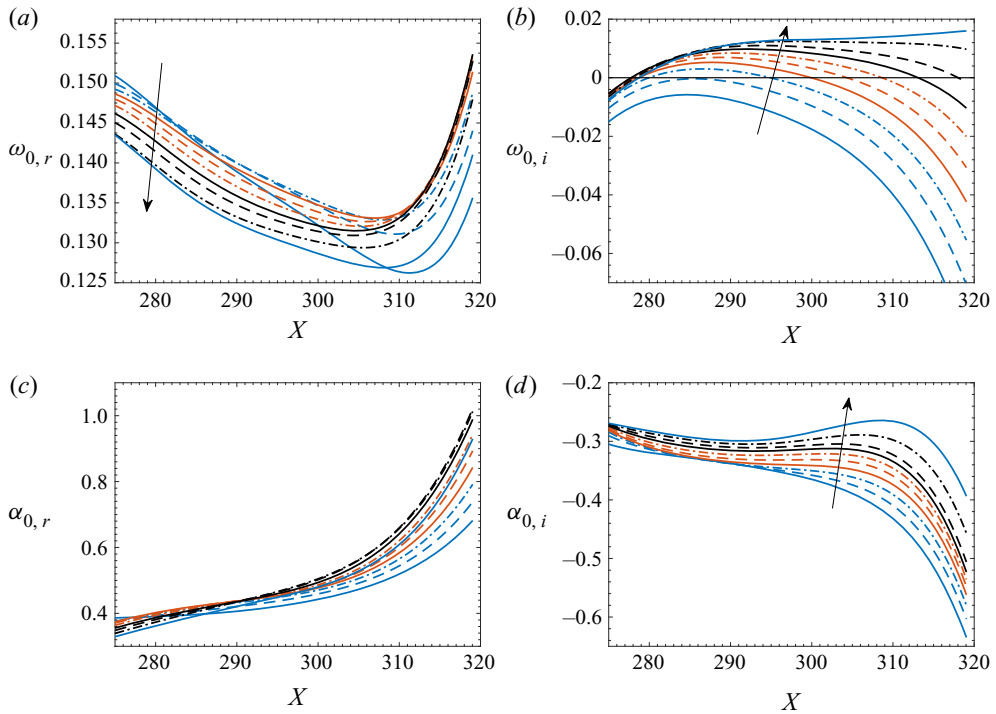


FIGURE 8. Absolute frequency and wavenumber of three-dimensional bubbles \bar{q}_{3D} . (a,b) Real and imaginary parts of the absolute frequency ω_0 . (c,d) Real and imaginary parts of the wavenumber α_0 . The lines correspond to (in the direction of the arrows): $\delta_{max} = 6.8, 7, 7.2, 7.4, 7.8, 8, 8.2, 8.5$ and 8.7 ; respectively $u_{0,rev} = 7.29\%, 7.54\%, 7.81\%, 8.06\%, 8.31\%, 8.56\%, 8.80\%, 9.04\%, 9.37\%$ and 9.57% .

comparable in amplitude to the convergence error of the steady flows just mentioned. The low-amplitude error ensures that any transient evolution resulting from switching off the SFD does not contaminate the solution hiding the linear phase of growth of the secondary instability. The time step used in the simulations in § 4 is reduced to ensure convergence of the results: simulations with $\Delta t = 0.78/16 \approx 4.88 \times 10^{-2}$ and $\Delta t = 0.78/32 \approx 2.44 \times 10^{-2}$ were carried out. Regarding this section, the results of both simulations are virtually identical.

Figure 11(a) shows the temporal evolution of the disturbance streamwise velocity at $(x, y, z) = (310, 1.75, 0)$, for a case in which the secondary instability is active. This location corresponds to a point within the recirculation region at the symmetry plane, slightly downstream of the wavemaker predicted by the WKBJ analysis (see figure 10). In what follows, the velocity probed at this point is denoted by $u^*(t)$. As opposed to the validation of the primary instability (§ 4.2), the disturbance flow field corresponding to the secondary instability is not imposed now, and some evolution time is required until a modal behaviour is reached. The temporal lapse in which the oscillations evolve linearly, as well as their complex frequency, are estimated from $u^*(t)$ as follows. First, the times corresponding to local maxima and minima ($t_{max,n}$ and $t_{min,n}$) are tracked, as denoted by circles and squares in figure 11(a). Each oscillation period n is defined as starting at a maximum (or minimum) and ending at the next one. The period-wise mean value of the signal, $u_{m,n}^*$ is also computed and shown by the dashed line in the figure. The mean value remains approximately equal to $u^*(t_0)$ for a long time lapse, eventually departing from

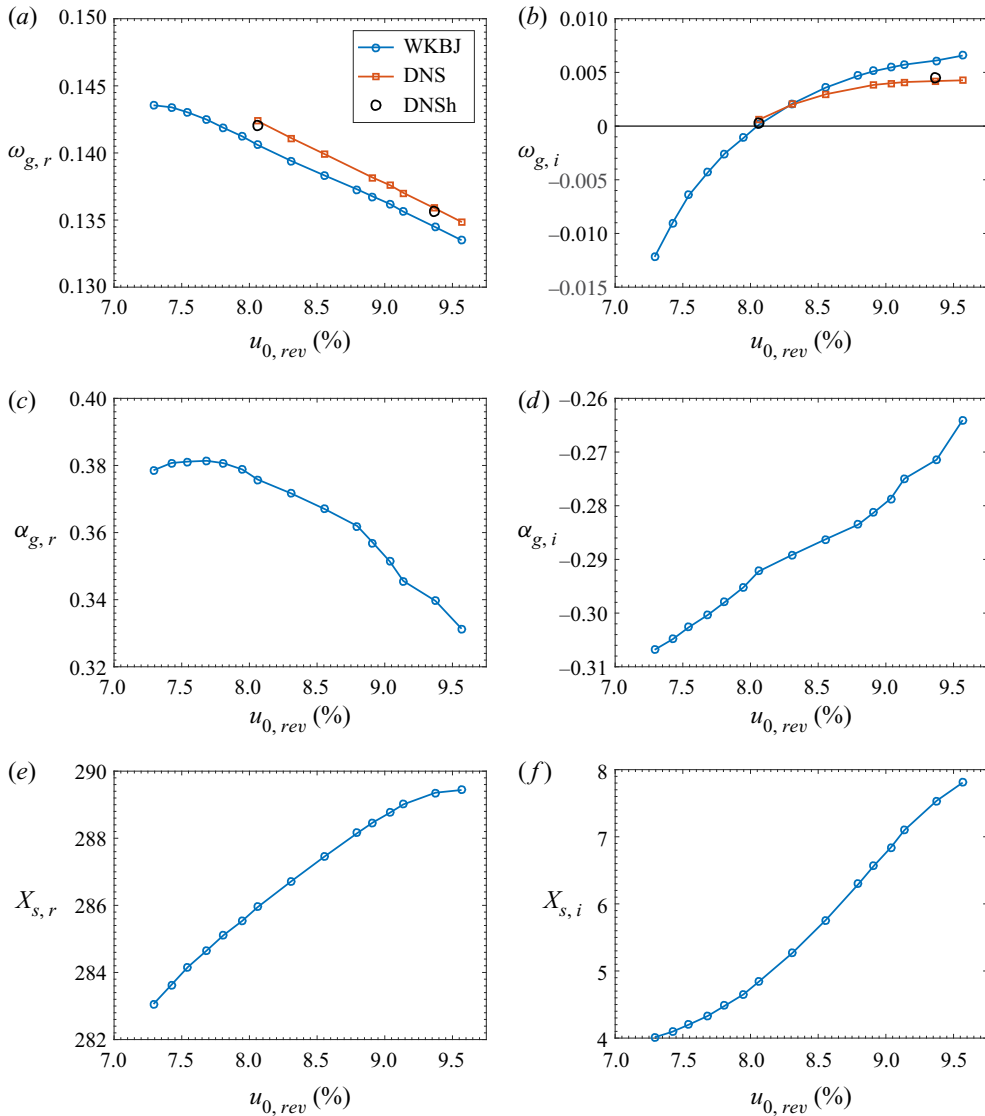


FIGURE 9. Properties of the secondary instability global oscillator computed using the cross-planes WKBJ analysis. (a,b) Real and imaginary parts of the global frequency ω_g . (c,d) Real and imaginary parts of the wavenumber α_g . (e,f) Real and imaginary parts of the wavenumber location X_s . The complex frequencies estimated from DNS is also shown in (a,b).

it, which indicates nonlinear effects and the deviation from the modal behaviour. The oscillation frequency is estimated for each period as $\omega_{r,n} = 2\pi / (t_{max,n+1} - t_{max,n})$, and an analogous expression for the minima. The growth rate is estimated by assuming a linear growth of the local maxima or minima about the period mean value $u_{m,n}^*$

$$\omega_{i,n} = \ln \left(\frac{u^*(t_{max,n+1}) - u_{m,n}^*}{u^*(t_{max,n}) - u_{m,n}^*} \right) / (t_{max,n+1} - t_{max,n}), \quad (5.1)$$

and similarly for the minima.

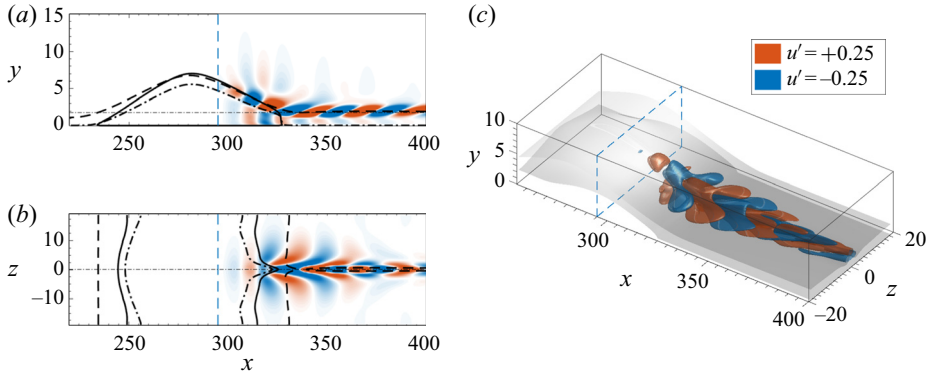


FIGURE 10. Spatial structure of the secondary instability global oscillator. Disturbance streamwise velocity u' at plane $z = 0$ (a), and at plane $y = 1.75$ (b). (c) Isocontours $u' = \pm 0.25$. Dashed-dotted, dashed and solid lines in (a,b) correspond to y_r , y_i and y_d , respectively. The grey surfaces in (c) correspond to y_d and $\bar{u}_{3D} = 0.5$. The thin dashed lines correspond to the real coordinate of the wavemaker. Baseline LSB corresponding to $\bar{\delta}_{max} = 8.5$, $u_{0,rev} = 9.37\%$.

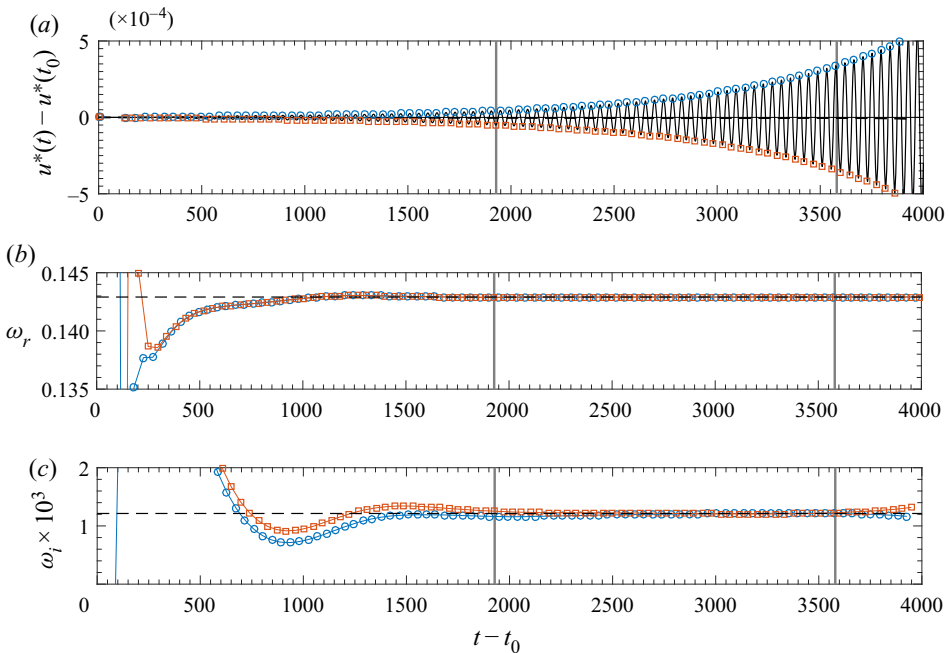


FIGURE 11. Cross-validation of the secondary instability. (a) Temporal evolution of the streamwise velocity at $(x, y, z) = (310, 1.75, 0)$. (b) Estimation of the frequency ω_r . (c) Estimation of the growth rate ω_i . Baseline LSB corresponds to $\bar{\delta}_{max} = 8.5$, $u_{0,rev} = 9.37\%$. Circles and squares correspond to local maxima and minima.

The estimates of the complex frequency are shown in figure 11(b,c). The quantities are considered converged when their relative variations over a period are lower than 10^{-3} , which occurs for $(t - t_0) \sim 1928$ for the case of the figure. Additionally, nonlinear effects are considered here to become relevant when the relative difference of $u_{m,n}^*$ and $u^*(t_0)$ is

larger than 10^{-3} . For the case shown in [figure 11](#), this occurs for $(t - t_0) \gtrsim 3580$. The time lapse of modal evolution is bounded between these two instants, represented by the vertical lines in the figure, and hence is limited to a finite number of oscillations, which strongly depends on the growth rate. The estimates based on maxima and minima deliver consistent results during this time lapse, and their mean values (the dashed lines in [figure 11b,c](#)) are taken as the modal complex frequency. The same complex frequencies are consistently recovered analysing the velocity at other probe locations within the reversed flow, and also considering the peak velocity of the spanwise-average Fourier mode, $\|\tilde{u}_0\|_\infty$, as shown in [figure 3](#).

The complex frequencies calculated from the DNS are compared to those predicted by the linear WKBJ analysis in [figure 9](#), showing a good agreement. Results of simulations with the increased spatial resolution $N_x \times N_y \times N_z = 1201 \times 241 \times 128$ and the time step $\Delta t = 0.78/32 \approx 2.44 \times 10^{-2}$ (DNSh) are also shown in the figure. The simulations recover frequencies that are consistently higher than the WKBJ ones. Similar deviations between the predictions of a WKBJ analysis and a global eigenmode analysis were identified by Siconolfi *et al.* (2017) for the wake of a circular cylinder. This quantitative deviation might be attributed to the limitation of the weakly non-parallel analysis when applied to flows with moderate non-parallelism. The spatial structure of the disturbances that develop in the simulations during the initial phase of linear growth agrees with the theoretical one (cf. [figures 10b](#) and [12b](#)).

6. Nonlinear development and transition to turbulence

The primary and secondary self-excited instabilities described in the previous sections give rise to the onset of three-dimensionality and unsteadiness in model laminar separation bubbles. This section illustrates qualitatively the nonlinear development of the flow field subsequent to the activation of the global oscillator, towards a complete laminar–turbulent transition.

[Figure 12\(a\)](#) shows the spatio-temporal evolution of the disturbance streamwise velocity $u'(x, t) - u'(x, t_0)$ for $(y, z) = (1.75, 0)$. The data correspond to the same simulation as [figure 11](#). [Figures 12\(b\)–12\(f\)](#) show the disturbance velocity at different instants of time. Note that the contour levels are varied from case to case, to allow for the visualization of the structures.

As a result of the secondary instability, the flow field develops synchronized oscillations that grow in amplitude until important nonlinear effects appear. For a relatively long time lapse, the disturbance flow field retains the features of the linear oscillator, at least in the vicinity of the reattachment line ([figures 12b](#) and [12c](#)). Downstream, the spatial structure gradually becomes more elongated on the streamwise direction, eventually becoming reminiscent of the Λ -structures identified by Alam & Sandham (2000) or Marxen & Rist (2010) ([figure 12d](#)). The formation and breakdown of the Λ -structures triggers a sudden transition to the turbulent regime, as shown in [figure 12\(e\)](#). Afterwards, strong nonlinear fluctuations dominate the flow field, including the aft part of the mean recirculation region. The well-organized structure of the linear global oscillator cannot be identified visually in the instantaneous velocity fields downstream of reattachment, but the periodic shedding of vortices from the separation bubble is still present, as evidenced by the later times in [figure 12\(a\)](#). A similar scenario was reported by Cherubini *et al.* (2010b), which is described in that work as the breakdown of Görtler modes due to a convective instability. The authors introduced an impulsive forcing upstream of the separation bubble, that initiated the development of a wavepacket. The subsequent nonlinear evolution triggered

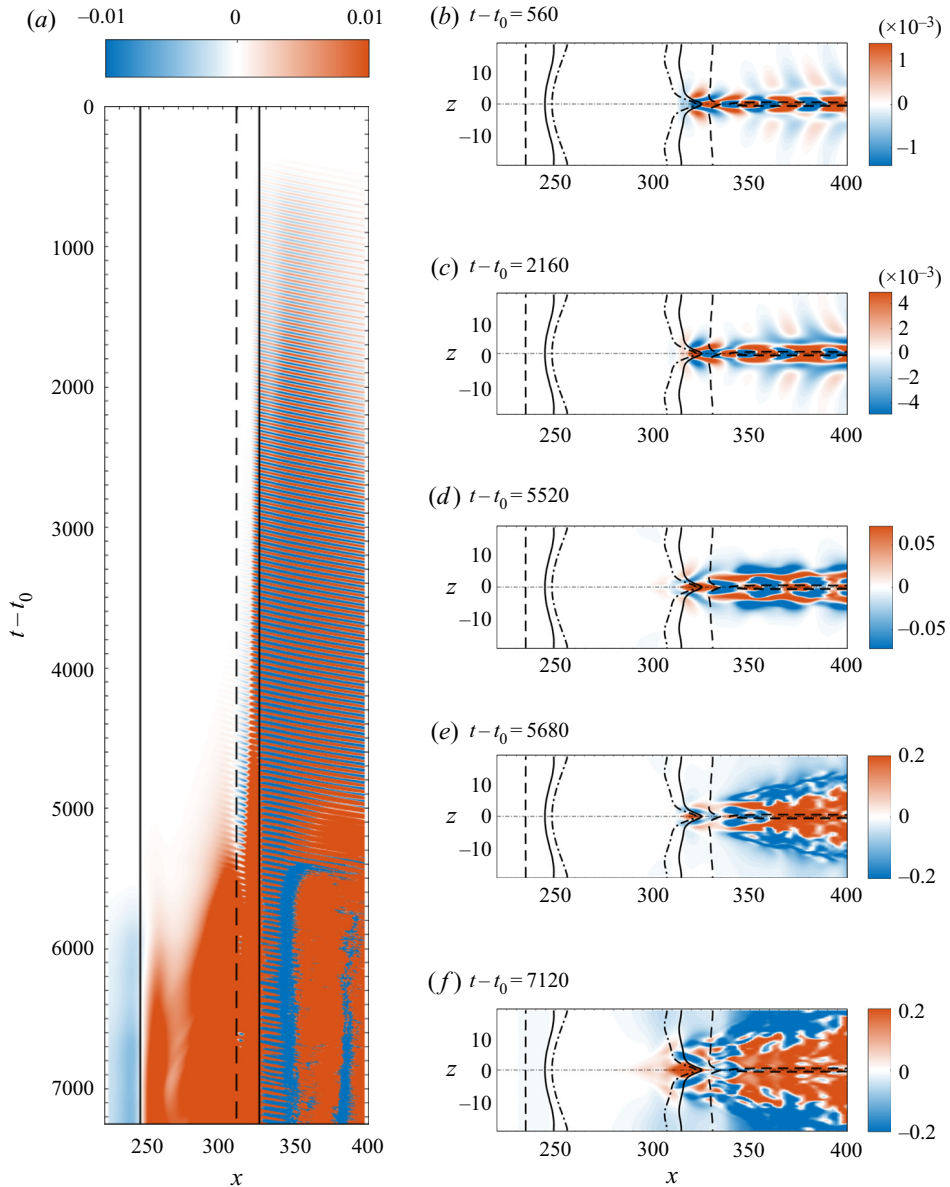


FIGURE 12. (a) Temporal evolution of the disturbance streamwise velocity $u' - u'(t_0)$ at $(y, z) = (1.75, 0)$. The vertical dashed line shows the location of the wavemaker X_s , as predicted by the WKBJ analysis, while solid lines show the location of y_d . (b–f) Instantaneous disturbance streamwise velocity $u' - u'(t_0)$ at $y = 1.75$ at different times. Dashed-dotted, dashed and solid lines correspond to y_r , y_i and y_d , respectively. Baseline LSB corresponding to $\delta_{max} = 8.5$, $u_{0,rev} = 9.37\%$.

the laminar–turbulent transition. In the present work, the transition is initiated by a linear global oscillator, resulting from the absolute instability of Kelvin–Helmholtz waves, and does not require of external forcing. It is also worth noting that frequency beating or flapping, as those reported by Ehrenstein & Gallaire (2008) and Cherubini *et al.* (2010a),

is not observed here (figures 11a and 12). This is consistent with the absence of unstable two-dimensional eigenmodes as shown in Rodríguez *et al.* (2013b) and appendix A.

7. Discussion and conclusions

This paper studies the linear and nonlinear instability processes that transform a steady, two-dimensional model recirculating flow into a fully three-dimensional and unsteady laminar separation bubble. The theoretical and numerical set-up does not introduce explicit forcing or free-stream disturbances, and thus the origin of three-dimensionality, unsteadiness and the eventual transition to turbulence can be associated with self-excited instabilities of the flow. Under these conditions, the primary instability exerts a spanwise modulation of the recirculation region. Direct numerical simulations are used to show that this instability corresponds to a supercritical pitchfork bifurcation. The growth of the spanwise-periodic modulation saturates at finite amplitudes, giving rise to fully three-dimensional steady flows. These bifurcated flows present spanwise-average peak reversed flows below 7% in all cases considered, lower than those of their respective baseline flows. Simultaneously, localized pockets with reversed flow exceeding 15% also appear. In the vicinity of these pockets, the local inflection point is located below the zero streamwise mass-flux line, satisfying the necessary condition for the absolute instability of Kelvin–Helmholtz waves suggested by Avanci *et al.* (2019).

A weakly non-parallel analysis based on cross-stream planes is applied to the bifurcated flows. As anticipated by the topological changes induced by the primary instability, the spanwise distortion of the separated shear layer is found to destabilize the varicose (symmetric) K–H waves, in line with the analyses by Saxena *et al.* (1999), Kawahara *et al.* (2003) and Marant & Cossu (2018). Absolute instability appears for baseline LSBs with reversed flow $u_{0,rev} \geq 7.29\%$, which is marginally larger than the critical $u_{0,rev} \geq 7.01\%$ for the primary instability, and a global oscillator becomes self-sustained for $u_{0,rev} \geq 8.1\%$. In practice, it can be expected that once the separated flow becomes three-dimensional, the spanwise modulation is sufficient to trigger the secondary instability. While in the present case the three-dimensionality is caused by the self-excited primary instability, similar scenarios can appear when external disturbances are allowed. For instance, if streamwise streaks of sufficient amplitude are present (e.g. Marxen & Rist 2010; Balzer & Fasel 2016; Karaca & Gungor 2016; Hosseinverdi & Fasel 2019; Li & Yang 2019), the spanwise distortion of the separated flow induced by them can lead to an absolute instability. This instability and the vortical structures resulting from it would appear in an unsteady and chaotic manner, following the nature of the streaks. Similarly, the absolute instability can appear in recirculation bubbles that are three-dimensional due to the geometry, as in indented boundary layers (Xu *et al.* 2017) or downstream of large roughness elements (Loiseau *et al.* 2014).

The present results may help to explain why unforced laminar separation bubbles with relatively low peak reversed flows exhibit dynamics that is expected only for ‘stronger’ LSBs, such as self-sustained shedding of three-dimensional vortical structures. The baseline LSBs subject of analysis here are inherently unstable for $u_{0,rev} \geq 7.01\%$; beyond this value, the sequence of self-excited instabilities presented leads to a separation bubble with turbulent reattachment and with a substantially lower time- and spanwise-average reversed flow. In general, numerical simulations or wind-tunnel experiments only allow the observation of the ‘final state’, resulting from the sequence of bifurcations. Applying stability analyses to these flows would deliver misleading results regarding the instability processes at play.

	$Re_{\theta,s}$	Re_L	u_{rev}	Tu
Watmuff (1999)	387	94 160	$\geq 7\%$	$< 0.1\%$
Serna & Lázaro (2014)	200–400	40 000–60 000	2%–15%	$< 0.1\%$
Kurelek <i>et al.</i> (2016)	204	28 000	$\sim 7.5\%$	$< 0.2\%$
Simoni <i>et al.</i> (2017)	90–116	11 700–20 250	$< 15\%$	0.65%–1.2%
Michelis <i>et al.</i> (2018)	532	64 000	$\sim 2\%$	$< 0.2\%$
Kurelek <i>et al.</i> (2018, 2019)	180	26 600	$\sim 4\%$	$< 0.1\%$
Present (baseline q_0)	208–212	37 600–40 500	$< 12\%$	
	λ_x/θ_s	λ_z/θ_s	λ_z/λ_x	St_θ
Watmuff (1999)	50.8*	123*	2.42*	0.008654
Serna & Lázaro (2014, 2015)	25–35	—	—	0.01–0.012
Kurelek <i>et al.</i> (2016)	35.1	71.4	2.00	0.017
Simoni <i>et al.</i> (2017)	59–63	—	—	0.013–0.016
Michelis <i>et al.</i> (2018)	34.8	67.4	1.94	0.01
Kurelek <i>et al.</i> (2018, 2019)	32	72	2.25	0.016
Present	31.0–37.9	76.3–76.9	2.06–2.41	0.01–0.012

TABLE 1. Comparison of various parameters characterizing the laminar separation bubbles in wind-tunnel experiments and present results: Reynolds number based on momentum thickness at separation $Re_{\theta,s}$; Reynolds number based on streamwise length of the recirculation region Re_L ; peak reversed flow u_{rev} ; free-stream turbulence intensity Tu ; dominant streamwise and spanwise wavelengths λ_x/θ_s , λ_z/θ_s of coherent structures and Strouhal number St_θ .

Some salient features of the resulting LSBs are in good agreement with those reported for quiet wind-tunnel experiments in which no forcing is applied externally, as shown in table 1. The quantities characterizing the mean LSB are also shown. The global oscillator frequency is compared to the reported vortex shedding frequencies in terms of the Strouhal number defined with the momentum thickness θ_s^* and free-stream velocity $U_{e,s}^*$ at separation, as defined by Pauley *et al.* (1990)

$$St_\theta = \frac{f^* \theta_s^*}{U_{e,s}^*}, \quad (7.1)$$

where f^* is the frequency in cycles per second. Streamwise and spanwise periodicity lengths scaled with θ_s^* , and the ratio between them, λ_z/λ_x , are also compared when possible. Note that some of the original references do not report the quantities using the same scaling used here. In some cases, the authors of the original references kindly provided the necessary information. In others, the quantities in table 1 have been determined based on the available data. In the case of Watmuff (1999), the quantities in the three first columns were roughly estimated from figures in the original paper and may have significant errors. Also note that the experiments by Kurelek *et al.* (2016, 2018, 2019) consider a NACA 0018 airfoil instead of a flat plate, which may originate the consistent difference in St_θ . It is stressed that the table only includes experimental results without explicit forcing like spanwise spacers, vibrating ribbons or unsteady suction–blowing. For those references in which disturbances are forced, the quantities shown here correspond to the reported natural conditions, before the introduction of the disturbances.

The frequency predicted for the global oscillator, $St_\theta = 0.01\text{--}0.012$, is in good agreement with the dominant vortex shedding frequency reported for experiments in a flat plate by Serna & Lázaro (2014, 2015) and Michelis *et al.* (2018). The flat-plate experiments by Simoni *et al.* (2017) and on the airfoil by Kurelek *et al.* (2016, 2018, 2019) present slightly higher frequencies ($St_\theta = 0.013\text{--}0.017$), which could be related to the relatively smaller Reynolds number. Conversely, Watmuff (1999) presents a lower $St_\theta = 0.008654$, and higher Re_L . The global oscillator frequency is also in good agreement with the vortex shedding frequency ($St_\theta = 0.0134\text{--}0.0136$) recovered in the three-dimensional unforced numerical simulations by Pauley (1994). Noticeably, this frequency is approximately twice the ‘universal’ $St_\theta = 0.0069$ frequency that was proposed by Pauley *et al.* (1990) for two-dimensional simulations and was also recovered by Alizard *et al.* (2009).

The characteristic wavelengths are also found to depend mildly on the Reynolds number. The aspect ratio is found to lie consistently in the range $\lambda_z/\lambda_x \sim 2\text{--}2.4$, either predicted for the global oscillator and in the unforced experiments. Incidentally, this aspect ratio is also in good agreement with the values reported by Rist & Augustin (2006) and Marxen & Henningson (2011). In these works, oblique Tollmien–Schlichting waves were introduced upstream of the separation bubbles. The relation between the streamwise and spanwise wavelengths for the largest spatial amplification was found to be 1.9 and 2.4, respectively. The reasons for this agreement with the present results are not clear.

Further work is required to shed light on the role of the primary and secondary self-excited instabilities discussed herein when environmental disturbances and/or explicit forcing are present. The plethora of possibilities span from the constructive interaction of disturbance waves existing in the pre-separated boundary layer with the inherent spanwise distortion of the LSB (as studied in Rodríguez & Gennaro 2019), to the formation of strongly coherent two-dimensional vortices by high-amplitude forcing (e.g. Embacher & Fasel 2014; Hosseinverdi & Fasel 2018), completely precluding the self-excited scenario.

Acknowledgements

The authors wish to thank J. Serna, T. Michelis, M. Dellacasagrande, D. Simoni and their respective co-authors for sharing their mean flow data and facilitating the comparisons done in §7. The authors acknowledge funding from the Brazilian agencies CNPq (grants 405144/2016-4, 305512/2016-1, 423846/2016-7), FAPESP (grants 2014/24782-0, 2017/01586-0) and FAPERJ (grants E-26/010.000356/2017 and E-26/200.003/2018).

Declaration of interests

The authors report no conflict of interest.

Appendix A. Cross-validation of the primary instability results

The growth or decay rate of the fundamental $k = 1$ modes recovered in the simulations is compared in figure 13(b) to the ones predicted by the eigenmode analysis. The excellent agreement between the results of two independent approaches with different spatial resolutions ensures the quality of the results.

A second validation test considers the behaviour of the $k \neq 1$ modes. As the unstable fundamental mode gradually attains higher amplitudes, nonlinear interactions excite the harmonics and the spanwise-average flow distortion. At a certain evolution time the nonlinear terms are switched off in the simulation allowing for the subsequent

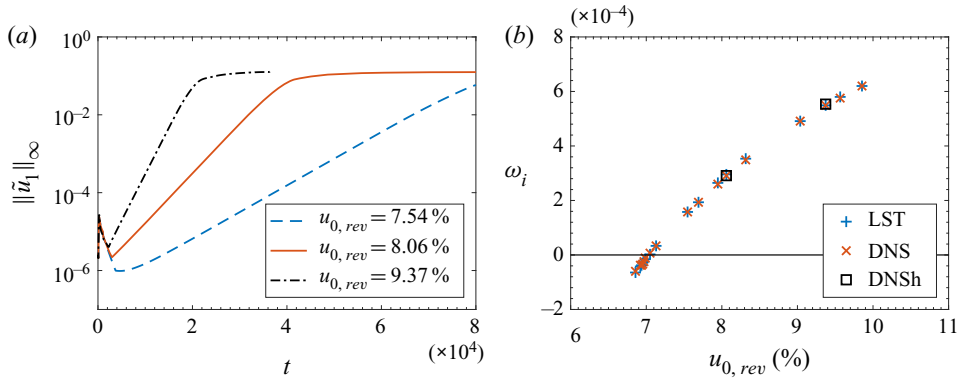


FIGURE 13. Cross-validation of linear growth rates in the primary instability. (a) Temporal evolution of the fundamental mode for different baseline LSBs. (b) Linear growth rates extracted from simulations (×) and predicted by linear stability analysis (+). Squares correspond to the DNSh simulations.

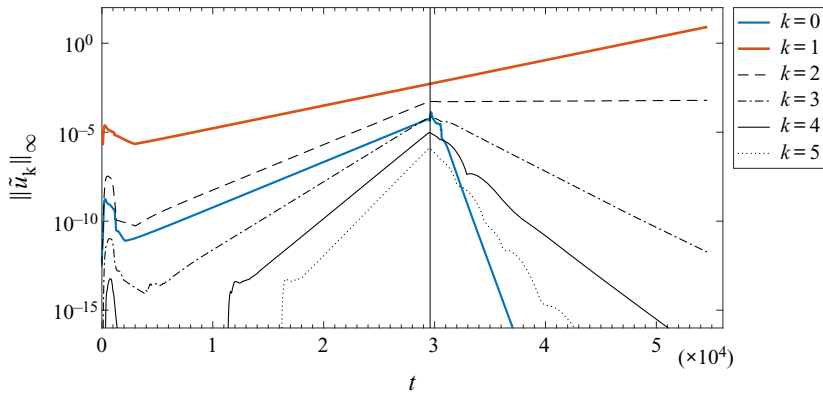


FIGURE 14. Temporal evolution of modal amplitudes during the initial development phase. Baseline LSB corresponds to $\delta_{max} = 7.4$, $u_{0,rev} = 8.06\%$. Nonlinear terms are switched off at $t = 2.96 \times 10^4$.

linear evolution of all modes (figure 14). All modes evolve following the growth rate predicted by the eigenmode analysis. The $k = 0$ mode decays monotonically, confirming that the baseline LSB is linearly stable with respect to two-dimensional disturbances. Consequently, shedding of two-dimensional vortices is not triggered by a self-sustained, linear oscillator-type instability for these flows, confirming the results of Rodríguez *et al.* (2013b).

Appendix B. On the need for a cross-stream plane analysis

Could a simpler one-dimensional eigenmode problem like the Orr–Sommerfeld equation be used to study the instability waves once the primary instability has exerted a finite-amplitude three-dimensionalization of the LSB? One difficulty would be the choice of a suitable base flow profile. The usual practice in the literature, stemming from neglecting the spanwise inhomogeneity of separation bubbles, is to consider the spanwise-average flow. This has been shown to deliver excellent predictions for forced

	ω_r	ω_i
\bar{q}_{3D} , cross-plane	0.14192584	4.8876421×10^{-3}
\bar{q}_{3D} , $z = 0$ profile	0.15391356	3.9755198×10^{-2}
\bar{q}_{2D} , $\beta = 0$	0.14994544	$-3.6978316 \times 10^{-2}$
Baseline q_0	0.14041469	$-4.6087438 \times 10^{-2}$

TABLE 2. Leading eigenmodes corresponding to the cross-plane of \bar{q}_{3D} and different spanwise-homogeneous approximations. The base flows used correspond to the $X = 286$ plane of the baseline LSB with $\delta_{max} = 7.4$, $u_{0,rev} = 8.06\%$, the respective bifurcated flows. The axial wavenumber is $\alpha = 0.42 - i0.33$.

convective waves (Gaster 1967; Dovgal *et al.* 1994; Diwan & Ramesh 2009; Marxen *et al.* 2012; Embacher & Fasel 2014; Michelis *et al.* 2017). In terms of the analysis, either the baseline undisturbed flow field q_0 or the spanwise average of the bifurcated flow \bar{q}_{2D} can be used. On the other hand, the spanwise modulation of the bifurcated flow leads to spanwise planes ($z = 0$ in \bar{q}_{3D}) with a peak reversed flow substantially higher than the spanwise average, and with the inflection point located within the recirculation region ($y_i < y_d$, see figure 6c,e,g). As the K–H instability is dominated by the properties of the base flow at the inflection point and becomes more unstable with increasing spanwise vorticity, the mechanism driving the disturbance growth is expected to be localized in this section; taking the profile $\bar{q}_{3D}(y; X, z = 0)$ is thus another reasonable possibility.

The latter three possible choices for the base velocity profile are tried and compared to the result of considering the complete cross-stream plane. The results are shown in table 2 for an illustrative case. While the frequency ω_r is predicted using spanwise-average analysis within a 5% relative error, important differences appear in the growth rate. The results for base profiles q_0 and \bar{q}_{2D} have $\omega_i < 0$. Conversely, the use of $\bar{q}_{3D}(y; X, z = 0)$ overestimates the growth rate by an order of magnitude. These results demonstrate that the cross-stream plane analysis is required on account of the spanwise inhomogeneity of the separated flow. Simplified analyses that assume the base flow spanwise homogeneity can underpredict the instability significantly.

REFERENCES

- ÅKERVIK, E., BRANDT, L., HENNINGSON, D. S., HOEPFFNER, J., MARXEN, O. & SCHLATTER, P. 2006 Steady solutions of the Navier–Stokes equations by selective frequency damping. *Phys. Fluids* **18**, 068102.
- ALAM, M. & SANDHAM, N. D. 2000 Direct numerical simulation of ‘short’ laminar separation bubbles with turbulent reattachment. *J. Fluid Mech.* **410**, 1–28.
- ALBENSOEDER, S., KUHLMANN, H. C. & RATH, H. J. 2001 Three-dimensional centrifugal-flow instabilities in the lid-driven cavity problem. *Phys. Fluids* **13**, 121–135.
- ALIZARD, F., CHERUBINI, S. & ROBINET, J. C. 2009 Sensitivity and optimal forcing response in separated boundary layer flows. *Phys. Fluids* **21**, 064108.
- ALLEN, T. & RILEY, N. 1995 Absolute and convective instabilities in separation bubbles. *Aeronaut. J.* **99**, 439–448.
- AMESTOY, P. R., DUFF, I. S., L’EXCELLENT, J.-Y. & KOSTER, J. 2001 A fully asynchronous multifrontal solver using distributed dynamic scheduling. *SIAM J. Matrix Anal. Applics.* **23** (1), 15–41.
- ARBEBY, H. & BATAILLE, J. 1983 Noise generated by airfoil profiles placed in a uniform laminar flow. *J. Fluid Mech.* **134**, 33–47.

- AVANCI, M. P., RODRÍGUEZ, D. & ALVES, L. S. B. 2019 A geometrical criterion for absolute instability in laminar separation bubbles. *Phys. Fluids* **31**, 014103.
- BAGHERI, S., SCHLATTER, P., SCHMID, P. J. & HENNINGSON, D. S. 2009 Global stability of a jet in crossflow. *J. Fluid Mech.* **624**, 33–44.
- BALZER, W. & FASEL, H. F. 2016 Numerical investigation of the role of free-stream turbulence in boundary-layer separation. *J. Fluid Mech.* **801**, 289–321.
- BARKLEY, D., GOMES, M. G. M. & HENDERSON, R. D. 2002 Three-dimensional instability in a flow over a backward-facing step. *J. Fluid Mech.* **473**, 167–190.
- BEAUDOIN, J. F., CADOT, O., AIDER, J. L. & WESFREID, J. E. 2004 Three-dimensional stationary flow over a backward-facing step. *Eur. J. Mech. B/Fluids* **23**, 147–155.
- BIPPES, H. & TURK, M. 1980 Windkanalmessungen in einem Rechteckflügel bei anliegender und abgelöster Strömung. *Tech. Rep.* DFVLR Forschungsbericht IB 251-80 A 18.
- BRÈS, G. A. & COLONIUS, T. 2008 Three-dimensional instabilities in compressible flow over open cavities. *J. Fluid Mech.* **599**, 309–339.
- CARTER, J. E. 1975 Inverse solutions for laminar boundary-layer flows with separation and reattachment. *Tech. Rep.* NASA TR R-447. NASA.
- CHERUBINI, S., ROBINET, J. C. & DE PALMA, B. 2010a The effects of non-normality and nonlinearity of the Navier–Stokes operator on the dynamics of a large laminar separation bubble. *Phys. Fluids* **22**, 014102.
- CHERUBINI, S., ROBINET, J. C., DE PALMA, B. & ALIZARD, F. 2010b The onset of three-dimensional centrifugal global modes and their nonlinear development in a recirculating flow over a flat-surface. *Phys. Fluids* **22**, 114102.
- CHOMAZ, J. M., HUERRE, P. & REDEKOPP, L. G. 1988 Bifurcation to local and global modes in spatially developing flows. *Phys. Rev. Lett.* **60**, 25–28.
- DALLMANN, U. & SCHEWE, G. 1987 On topological changes of separating flow structures at transition reynolds numbers. In *16th Fluid Dynamics, Plasma Dynamics and Lasers Conference, AIAA Paper* 87-1266.
- DIWAN, S. S., CHETAN, S. J. & RAMESH, O. N. 2006 On the bursting criterion for laminar separation bubbles. In *Sixth IUTAM Symposium on Laminar-turbulent Transition* (ed. R. Govindarajan), pp. 401–407. Springer.
- DIWAN, S. S. & RAMESH, O. N. 2009 On the origin of the inflectional instability of a laminar separation bubble. *J. Fluid Mech.* **629**, 263–298.
- DIWAN, S. S. & RAMESH, O. N. 2012 Relevance of local parallel theory to the linear stability of laminar separation bubbles. *J. Fluid Mech.* **698**, 468–478.
- DIWAN, S. S. 2009 Dynamics of early stages of transition in a laminar separation bubble. PhD thesis, Indian Institute of Science, Bangalore, India.
- DOVGAL, A. V., KOZLOV, V. V. & MICHALKE, A. 1994 Laminar boundary layer separation: instability and associated phenomena. *Prog. Aerosp. Sci.* **3**, 61–94.
- EHRENSTEIN, U. & GALLAIRE, F. 2008 Two-dimensional global low-frequency oscillations in a separating boundary-layer flow. *J. Fluid Mech.* **614**, 315–327.
- EMBACHER, M. & FASEL, H. F. 2014 Direct numerical simulations of laminar separation bubbles: investigation of absolute instability and active flow control of transition to turbulence. *J. Fluid Mech.* **747**, 141–185.
- FASEL, H. F. & POSTL, D. 2004 Interaction of separation and transition of three-dimensional development in boundary layer transition. In *Sixth IUTAM Symposium on Laminar-Turbulent Transition* (ed. R. Govindarajan), pp. 71–88. Springer.
- FELDMAN, Y. & GELFGAT, A. Y. 2010 Oscillatory instability of a 3D lid-driven flow in a cube. *Phys. Fluids* **22**, 093602.
- GALLAIRE, F., MARQUILLIE, M. & EHRENSTEIN, U. 2007 Three-dimensional transverse instabilities in detached boundary layers. *J. Fluid Mech.* **571**, 221–233.
- GASTER, M. 1963 On the instability of parallel shear layers and the behaviour of laminar separation bubbles. PhD thesis, Queen Mary College, London.
- GASTER, M. 1967 The structure and behaviour of separation bubbles. *Tech. Rep.* 3595, NPL Rep. & Memoranda.

- GASTER, M. 2004 Laminar separation bubbles. In *Sixth IUTAM Symposium on Laminar-Turbulent Transition* (ed. R. Govindarajan), pp. 1–13. Springer.
- GENNARO, E. M., RODRÍGUEZ, D., MEDEIROS, M. A. F. & THEOFILIS, V. 2013 Sparse techniques in global flow instability with application to compressible leading-edge flow. *AIAA J.* **51** (9), 2295–2303.
- GENNARO, E. M., SOUZA, B. D. P. & RODRÍGUEZ, D. 2019 The effect of compressibility on the primary global instability of unforced laminar separation bubbles. *J. Braz. Soc. Mech. Sci. Engng* **41** (12), 559.
- GIANNETTI, F. & LUCHINI, P. 2007 Structural sensitivity of the first instability of the cylinder wake. *J. Fluid Mech.* **581**, 167–197.
- GÓMEZ, F., CLAINCHE, S. LE, PAREDES, P., HERMANN, M. & THEOFILIS, V. 2012 Four decades of studying global linear instability: progress and challenges. *AIAA J.* **50** (12), 2731–2743.
- HAMMOND, D. A. & REDEKOPP, L. G. 1998 Local and global instability properties of separation bubbles. *Eur. J. Mech. B/Fluids* **17**, 145–164.
- HORNUNG, H. G. & PERRY, A. E. 1984 Some aspects of three-dimensional separation. Part I. Stream surface bifurcations. *Z. Flugwiss. Weltraumforsch.* **8**, 77–87.
- HOSSEINVERDI, S. & FASEL, H. F. 2013 Direct numerical simulations of transition to turbulence in two-dimensional laminar separation bubbles. In *51st AIAA Aerospace Sciences Meeting, AIAA Paper 2013-0264*.
- HOSSEINVERDI, S. & FASEL, H. F. 2018 Role of klebanoff modes in active flow control of separation: direct numerical simulation. *J. Fluid Mech.* **850**, 954–983.
- HOSSEINVERDI, S. & FASEL, H. F. 2019 Numerical investigation of laminar-turbulent transition in laminar separation bubbles: the effect of free-stream turbulence. *J. Fluid Mech.* **858**, 714–759.
- HOWARTH, L. 1934 On calculation of the steady flow in the boundary layer near the surface of a cylinder in a stream. *A.R.C. Reports and Memoranda* 1632.
- HUERRE, P. & MONKEWITZ, P. A. 1990 Local and global instabilities in spatially developing flows. *Annu. Rev. Fluid Mech.* **22**, 473–537.
- JONES, B. M. 1934 Stalling. *J. R. Aero. Soc.* **38**, 747–770.
- JONES, L. E., SANDBERG, R. D. & SANDHAM, N. D. 2008 Direct numerical simulations of forced and unforced separation bubbles on an airfoil at incidence. *J. Fluid Mech.* **602**, 175–207.
- JORDI, B. E., COTTER, C. J. & SHERWIN, S. J. 2014 Encapsulated formulation of the selective frequency damping method. *Phys. Fluids* **26**, 034101.
- JUNIPER, M. P. & PIER, B. 2015 The structural sensitivity of open shear flows calculated with a local stability analysis. *Eur. J. Mech. B/Fluids* **49**, 426–437.
- JUNIPER, M. P., TAMMISOLA, O. & LUNDELL, F. 2011 The local and global stability of confined planar wakes at intermediate reynolds number. *J. Fluid Mech.* **686**, 218–238.
- KARACA, S. & GUNGOR, A. G. 2016 DNS of unsteady effects on the control of laminar separated boundary layers. *Eur. J. Mech. B/Fluids* **56**, 71–81.
- KAWAHARA, G., JIMÉMEZ, J., UHLMANN, M. & PINELLI, A. 2003 Linear instability of a corrugated vortex sheet – a model for streak instability. *J. Fluid Mech.* **483**, 315–342.
- KITSIOS, V., RODRÍGUEZ, D., THEOFILIS, V., OOI, A. & SORIA, J. 2009 Biglobal stability analysis in curvilinear coordinates of massively separated lifting bodies. *J. Comput. Phys.* **228**, 7181–7196.
- KLOKER, M. & KONZELMANN, U. 1993 Outflow boundary conditions for spatial Navier–Stokes simulations of transitional boundary layers. *AIAA J.* **31**, 620–628.
- KURELEK, J. W., KOTSONIS, M. & YARUSEVYCH, S. 2018 Transition in a separation bubble under tonal and broadband acoustic excitation. *J. Fluid Mech.* **853**, 1–36.
- KURELEK, J. W., KOTSONIS, M. & YARUSEVYCH, S. 2019 Vortex merging in a laminar separation bubble under natural and forced conditions. *Phys. Rev. Fluids* **4**, 063903.
- KURELEK, J. W., LAMBERT, A. R. & YARUSEVYCH, S. 2016 Coherent structures in the transition process of a laminar separation bubble. *AIAA J.* **54** (8), 2295–2309.
- LELE, S. K. 1992 Compact finite difference schemes with spectral-like resolution. *J. Comput. Phys.* **103**, 16–42.
- LI, H. J. & YANG, Z. 2019 Separated boundary layer transition under pressure gradient in the presence of freestream turbulence. *Phys. Fluids* **31**, 104106.

- LINNICK, M. N. & FASEL, H. F. 2005 A high-order immersed interface method for simulating unsteady incompressible flows on irregular domains. *J. Comput. Phys.* **204**, 157–192.
- LOISEAU, J.-C., ROBINET, J.-C., CHERUBINI, S. & LERICHE, E. 2014 Investigation of the roughness-induced transition: global stability analysis and direct numerical simulations. *J. Fluid Mech.* **760**, 175–211.
- MARANT, M. & COSSU, C. 2018 Influence of optimally amplified streamwise streaks on the Kelvin–Helmholtz instability. *J. Fluid Mech.* **838**, 478–500.
- MARQUET, O., LOMBARDI, M., CHOMAZ, J. M., SIPP, D. & JACQUIN, L. 2009 Direct and adjoint global modes of a recirculation bubble: lift-up and convective non-normalities. *J. Fluid Mech.* **622**, 1–21.
- MARQUET, O., SIPP, D., CHOMAZ, J. M. & JACQUIN, L. 2008 Amplifier and resonator dynamics of a low-Reynolds-number recirculation bubble in a global framework. *J. Fluid Mech.* **605**, 429–443.
- MARQUILLIE, M. & EHRENSTEIN, U. 2003 On the onset of nonlinear oscillations in a separating boundary-layer flow. *J. Fluid Mech.* **490**, 169–188.
- MARXEN, O. & HENNINGSON, D. S. 2011 The effect of small-amplitude convective disturbances on the size and bursting of a laminar separation bubble. *J. Fluid Mech.* **671**, 1–33.
- MARXEN, O., LANG, M. & RIST, U. 2012 Discrete linear local eigenmodes in a separating laminar boundary layer. *J. Fluid Mech.* **711**, 1–26.
- MARXEN, O., LANG, M. & RIST, U. 2013 Vortex formation and vortex breakup in laminar separation bubbles. *J. Fluid Mech.* **728**, 58–90.
- MARXEN, O., LANG, M., RIST, U., LEVIN, O. & HENNINGSON, D. S. 2009 Mechanisms for spatial steady three-dimensional disturbance growth in a non-parallel and separating boundary layer. *J. Fluid Mech.* **634**, 165–189.
- MARXEN, O. & RIST, U. 2010 Mean flow deformation in a laminar separation bubble: separation and stability characteristics. *J. Fluid Mech.* **660**, 37–54.
- MCCULLOUGH, G. B. & GAULT, D. E. 1951 Examples of three representative types of airfoil-section stall at low speed. *TN 2502*, NACA.
- MICHELIS, T., YARUSEVYCH, S. & KOTSONIS, M. 2017 Response of a laminar separation bubble to impulsive forcing. *J. Fluid Mech.* **820**, 633–666.
- MICHELIS, T., YARUSEVYCH, S. & KOTSONIS, M. 2018 On the origin of spanwise vortex deformations in laminar separation bubbles. *J. Fluid Mech.* **841**, 81–108.
- MITRA, A. & RAMESH, O. N. 2019 New correlation for the prediction of bursting of a laminar separation bubble. *AIAA J.* **57** (4), 1400–1408.
- NASH, E. C., LOWSON, M. V. & MCALPINE, A. 1999 Boundary-layer instability noise on aerofoils. *J. Fluid Mech.* **382**, 27–61.
- PASSAGLIA, P.-Y., LEWEKE, T. & EHRENSTEIN, U. 2012 Transverse instability and low-frequency flapping in incompressible separated boundary layer flows: an experimental study. *J. Fluid Mech.* **703**, 363–373.
- PAULEY, L. P., MOIN, P. & REYNOLDS, W. C. 1990 The structure of two-dimensional separation. *J. Fluid Mech.* **220**, 397–411.
- PAULEY, L. L. 1994 Structure of local pressure-driven three-dimensional transient boundary-layer separation. *AIAA J.* **32** (5), 997–1005.
- PETRI, L. A., SARTORI, P., ROGENSKI, J. K. & DE SOUZA, L. F. 2015 Verification and validation of a direct numerical simulation code. *Comput. Meth. Appl. Mech. Engng* **291**, 266–279.
- PIER, B. 2002 On the frequency selection of finite-amplitude vortex shedding in the cylinder wake. *J. Fluid Mech.* **458**, 407–417.
- PIER, B. 2008 Local and global instabilities in the wake of a sphere. *J. Fluid Mech.* **603**, 39–61.
- REYHNER, T. A. & FLÜGGE-LOTZ, I. 1968 The interaction of a shock wave with a laminar boundary-layer. *Intl J. Non-Linear Mech.* **3** (2), 179–199.
- RIST, U. & AUGUSTIN, K. 2006 Control of laminar separation bubbles using instability waves. *AIAA J.* **44** (10), 2217–2223.

- RIST, U. & MAUCHER, U. 1994 Direct numerical simulation of 2-d and 3-d instability waves in a laminar separation bubble. In *AGARD-CP-551 Application of Direct and Large Eddy Simulation to Transition and Turbulence* (ed. B. Cantwell), pp. 34–1–7.
- RIST, U. & MAUCHER, U. 2002 Investigations of time-growing instabilities in laminar separation bubbles. *Eur. J. Mech. B/Fluids* **21**, 495–509.
- ROBINET, J. CH. 2007 Bifurcations in shock-wave/laminar-boundary-layer interaction: global instability approach. *J. Fluid Mech.* **579**, 85–112.
- ROBINET, J.-C. 2013 Instabilities in laminar separation bubbles. *J. Fluid Mech.* **732**, 1–4.
- RODRÍGUEZ, D. 2010 Global stability of laminar separation bubbles. PhD thesis, Universidad Politécnica de Madrid.
- RODRÍGUEZ, D. & GENNARO, E. M. 2015 On the secondary instability of forced and unforced laminar separation bubbles. *Procedia IUTAM* **14**, 78–87.
- RODRÍGUEZ, D. & GENNARO, E. M. 2017 Three-dimensional flow stability analysis based on the matrix-forming approach made affordable. In *International Conference on Spectral and High-Order Methods 2016* (ed. J. S. Hesthaven), Lecture Notes in Computational Science and Engineering. Springer.
- RODRÍGUEZ, D. & GENNARO, E. M. 2019 Enhancement of disturbance wave amplification due to the intrinsic three-dimensionalisation of laminar separation bubbles. *Aeronaut. J.* **123** (1268), 1492–1507.
- RODRÍGUEZ, D., GENNARO, E. M. & JUNIPER, M. P. 2013a On the two classes of global primary modal instability in laminar separation bubbles. *AIAA Paper* 2013-2621.
- RODRÍGUEZ, D., GENNARO, E. M. & JUNIPER, M. P. 2013b The two classes of primary modal instability in laminar separation bubbles. *J. Fluid Mech.* **734**, R4.
- RODRÍGUEZ, D. & THEOFILIS, V. 2010a On the birth of stall cells on airfoils. *Theor. Comput. Fluid Dyn.* **25**, 105–117.
- RODRÍGUEZ, D. & THEOFILIS, V. 2010b Structural changes of laminar separation bubbles induced by global linear instability. *J. Fluid Mech.* **655**, 280–305.
- SAXENA, V., LEIBOVICH, S. & BERKOOZ, G. 1999 Enhancement of three-dimensional instability of free shear layers. *J. Fluid Mech.* **379**, 23–38.
- SCHLICHTING, H. 1979 *Boundary Layer Theory*, 7th edn. McGraw-Hill.
- SCHMID, P. J. & HENNINGSON, D. S. 2001 *Stability and Transition in Shear Flows*. Springer.
- SERNA, J. & LÁZARO, B. J. 2014 The final stages of transition and the reattachment region in transitional separation bubbles. *Exp. Fluids* **55**, 1695.
- SERNA, J. & LÁZARO, B. J. 2015 On the bursting condition for transitional separation bubbles. *Aerosp. Sci. Technol.* **44**, 43–50.
- SICONOLFI, L., CITRO, V., GIANNETTI, F., CAMARRI, S. & LUCHINI, P. 2017 Towards a quantitative comparison between global and local stability analysis. *J. Fluid Mech.* **819**, 147–167.
- SIMONI, D., LENGANI, D., UBALDI, M., ZUNINO, P. & DELLACASAGRANDE, M. 2017 Inspection of the dynamic properties of laminar separation bubbles: free-stream turbulence intensity effects for different reynolds numbers. *Exp. Fluids* **58** (66), 1–14.
- SPALART, P. R. & STRELETS, M. KH. 2000 Mechanisms of transition and heat transfer in a separation bubble. *J. Fluid Mech.* **403**, 329–349.
- STRÜBEN, K. & TROTTEBERG, U. 1981 Lecture notes in mathematics. In *Nonlinear Multigrid Methods: the Full Approximation Scheme*, pp. 58–71. Köln-Porz.
- TEZUKA, A. & SUZUKI, K. 2006 Three-dimensional global linear stability analysis of flow around a spheroid. *AIAA J.* **44**, 1697–1708.
- THEOFILIS, V. 2011 Global linear stability. *Annu. Rev. Fluid Mech.* **43**, 319–352.
- THEOFILIS, V., DUCK, P. W. & OWEN, J. 2004 Viscous linear stability analysis of rectangular duct and cavity flows. *J. Fluid Mech.* **505**, 249–286.
- THEOFILIS, V., HEIN, S. & DALLMANN, U. 2000 On the origins of unsteadiness and three-dimensionality in a laminar separation bubble. *Phil. Trans. R. Soc. Lond. A* **358**, 3229–3246.
- DE VICENTE, J., BASLEY, J., MESEGUER-GARRIDO, F., SORIA, J. & THEOFILIS, V. 2014 Three-dimensional instabilities over a rectangular open cavity: from linear stability analysis to experimentation. *J. Fluid Mech.* **748**, 189–220.

- WATMUFF, J. H. 1999 Evolution of a wave packet into vortex loops in a laminar separation bubble. *J. Fluid Mech.* **397**, 119–169.
- XU, H., MUGHAL, S. M., GOWREE, E. R., ATKIN, C. J. & SHERWIN, S. J. 2017 Destabilisation and modification of Tollmien–Schlichting disturbances by a three-dimensional surface indentation. *J. Fluid Mech.* **819**, 592–620.
- ZAMAN, K. M. B. Q., MCKINZIE, D. J. & RUMSEY, C. L. 1989 A natural low-frequency oscillation of the flow over an airfoil near stalling conditions. *J. Fluid Mech.* **202**, 403–442.
- ZHANG, W. & SAMTANEY, R. 2016 Biglobal linear stability analysis on low-re flow past an airfoil at high angle of attack. *Phys. Fluids* **28**, 044015.